

Observational Properties of Thermal Emission from Relativistic Jets Embedded in AGN Disks

KEN CHEN¹ AND ZI-GAO DAI²

¹*School of Astronomy and Space Science, Nanjing University, Nanjing 210023, China*

²*Department of Astronomy, School of Physical Sciences, University of Science and Technology of China, Hefei 230026, China; daizg@ustc.edu.cn*

ABSTRACT

Relativistic jets can be produced within the accretion disk of an active galactic nucleus (AGN), leading to distinct thermal emission as they propagate through a dense disk environment. In this paper, we present a comprehensive study of dynamical evolution of jets embedded in an AGN disk and their associated observational properties, focusing on scenarios in which jets either successfully break out of the disk or become choked. By modeling the jet-cocoon system propagation, we calculate the thermal emission contributions from the jet-head shock breakout, disk cocoon, and jet cocoon components. Our results reveal that soft X-ray flares are the most prominent observable signatures, with duration ranging from $O(10^2)$ s to $O(10^5)$ s, occasionally exhibiting double-peaked light curves, whereas UV/optical flares are detectable only for powerful jets, persisting for several days to tens of days. This thermal emission serves as a critical electromagnetic counterpart to jet-producing events and provide insights into jet dynamics and AGN disk properties. Our findings highlight the importance of multi-wavelength follow-up observations to establish a diagnostic paradigm for candidate electromagnetic counterpart identification to AGN-embedded events and to distinguish thermal flares from AGN background variability.

Keywords: Active galactic nuclei (16); Accretion (14); Relativistic jets (1390)

1. INTRODUCTION

The accretion disk of an active galactic nucleus (AGN) serves as a cosmic laboratory for extreme astrophysical phenomena, many of which are associated with the production of relativistic jets. The AGN disk is predicted to harbor stars and compact objects (e.g. Syer et al. 1991; Goodman 2003; McKernan et al. 2012; Fabj et al. 2020; Jermyn et al. 2021; Fabj et al. 2025), In such an environment, the core-collapse of massive stars can generate jets powering long gamma-ray burst (GRB) (Woosley 1993; Woosley & Bloom 2006), while compact objects undergoing hyper-Eddington accretion processes are capable of launching jets (e.g. Tagawa et al. 2023a). Meanwhile, the AGN disk provides a plausible formation channel for gravitational wave (GW) events (e.g. Abbott et al. 2020; Tagawa et al. 2020; McKernan et al. 2020a,b; Perna et al. 2021b; Ishibashi & Gröbner 2024; Delfavero et al. 2024; Rowan et al. 2024). Binary neutron star mergers or neutron star-black hole mergers embedded in the AGN disk can produce jets that power short GRBs (e.g. Abbott et al. 2017a,a), whereas the remnants of binary black hole mergers can launch jets via accreting the ambient dense gas (e.g. Tagawa et al. 2023b, 2024; Rodríguez-Ramírez et al. 2024; Chen & Dai 2024). Tidal disruption events involving stellar-mass black holes in the AGN disk (Yang et al. 2022) could also produce jets similar to those observed in jetted tidal disruption events (e.g. Dai et al. 2018). Investigating the emission generated by jets embedded in AGN disks facilitates the prediction of electromagnetic (EM) counterparts of jet-producing systems, thereby enabling a better understanding of their properties. Simultaneously, jet emissions can provide valuable insights into the nature of the AGN disk.

Recently, several studies have explored the observational properties of two specific types of jets within AGN disks: GRB jets and GRB-less jets produced in binary black hole merger systems. For GRB jets, significant attention has been focused on the production and propagation of non-thermal radiation. Both the intrinsic properties of prompt emissions (e.g. Perna et al. 2021a; Lazzati et al. 2022; Kang et al. 2025) and afterglows (e.g. Wang et al. 2022; Kathirgamaraju et al. 2024; Huang et al. 2024; Kang et al. 2025) of embedded GRB jets differ substantially from typical cases (Zhang 2018). These non-thermal photons undergo frequent diffusion (e.g. Perna et al. 2021a; Wang

et al. 2022) and absorption (e.g. Ray et al. 2023) before escaping the disk photosphere, which further modifies the observed emissions. Additionally, Zhang et al. (2024) examined the dynamics of GRB jets within AGN disks and found that these jets are probably choked by the dense environment. On the other hand, the potential observation of jets from the remnants of binary black hole mergers is explored through analyzing their interaction with the AGN disk (Tagawa et al. 2023b, 2024; Chen & Dai 2024; Rodríguez-Ramírez et al. 2024). The resulting emissions originate from the jet-head successfully breaking out of the disk (Tagawa et al. 2023b; Chen & Dai 2024) and the subsequent expansion of shocked jet and disk materials (Tagawa et al. 2024; Chen & Dai 2024; Rodríguez-Ramírez et al. 2024). However, these studies have been confined to specific astrophysical events and each demonstrates certain limitations. For instance, some have oversimplified the interaction between the jet and the AGN disk, thereby neglecting the formation of the cocoon structure; some have failed to consider photon trapping within the opaque jet-cocoon system; while others have omitted a comprehensive evaluation of radiation contributions from all material components. Therefore, a systematic investigation that simultaneously address both jet propagation and observed radiation production becomes imperative and valuable.

In this paper, we investigate the observational properties of a relativistic jet with a power and a duration launched at different radius within various AGN disks. We calculate the entire propagation process of the jet until it breaks out of the AGN disk, focusing on the thermal emissions from the opaque jet-cocoon system generated by the interaction between the jet and the AGN disk. These emissions either serve as the first light of a successfully breaking-out jet or represent the sole signal of a choked jet. The paper is organized as follows. In Section 2, we describe the dynamics of jet propagation and investigate the properties of the jet-cocoon system, including the jet-choking criterion. In Section 3, we present a comprehensive analysis of the thermal emission from all components of the system, namely the jet-head shock breakout emission, the disk-cocoon emission, and the jet-cocoon emission. Additionally, we examine the emission mechanism in the jet-choking scenario. The observational properties of radiation produced by the embedded jet are outlined in Section 4, with particular emphasis on the detectability of these thermal emissions in Section 4.2. We summarize our main results and provide discussion in Section 5. Symbols G and c in this paper represents the gravitational constant and the speed of light, respectively.

2. JET PROPAGATION WITHIN AGN DISK

2.1. AGN Disk Structure

To investigate the propagation of jets in an AGN disk, it is essential to determine the vertical density profile of the disk gas. An accretion disk is commonly understood to maintain a vertical hydrostatic equilibrium between its pressure and gas self-gravity (Kato et al. 2008). Adopting a one-zone approximation to simplify the vertical structure, where the density is assumed to be uniform with $\rho_{\text{uni}}(z) = \rho_0$ and truncated at the disk surface of a scale height H_d , various models have been developed to characterize the structures of AGN disk (e.g. Sirko & Goodman 2003; Thompson et al. 2005; Gilbaum & Stone 2022; Chen & Lin 2024a; Gangardt et al. 2024; Epstein-Martin et al. 2025). Two more plausible vertical density profiles can be obtained by incorporating the specific pressure properties, one is the gas-pressure-dominated isothermal density profile (Kato et al. 2008)

$$\rho_{\text{iso}}(z) = \rho_0 \exp\left[-\frac{z^2}{2H_d^2}\right], \quad (1)$$

and another is the radiation-pressure-dominated polytropic density profile (Kato et al. 2008; Grishin et al. 2021)

$$\rho_{\text{poly}}(z) = \rho_0 \left(1 - \frac{z^2}{6H_d^2}\right)^3. \quad (2)$$

Both profiles indicate that the density is roughly uniform within H_d and drop sharply beyond H_d , suggesting a more diffuse structure compared to ρ_{uni} .

As the energy source for a supermassive black hole at the galactic center, both the mass of an AGN disk and its mass inflow rate must be sufficiently high to power a luminous active galactic nucleus. Although the AGN disk is generally geometrically thin with $H_d/R \ll 1$, where R is the disk radius, its actual vertical thickness combined with high density can result in an opaque gas environment. The vertical optical depth of the disk is given by

$$\tau_d(z) = \int_z^{z_{\text{edge}}} \kappa \rho(z') dz', \quad (3)$$

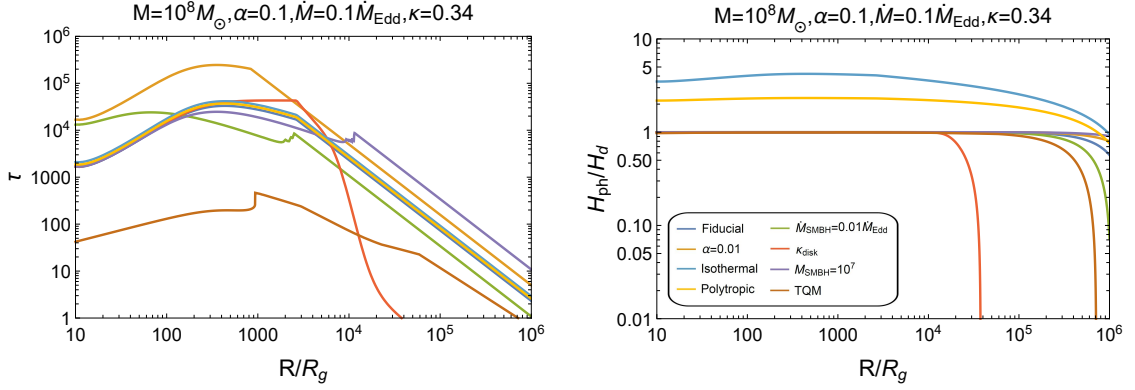


Figure 1. Vertical optical depth and photosphere height measured from the mid-plane of AGN disk. M is the mass of supermassive black hole (SMBH) in units of M_\odot , α is the viscosity parameter (Shakura & Sunyaev 1973), and R is the radius of AGN disk on scale of gravitational radius $R_g = GM/c^2$. The mass inflow rate of AGN disk is in units of the Eddington limit accretion rate, $\dot{M}_{\text{Edd}} = L_{\text{Edd}}/\eta c^2$, where $\eta = 0.1$ and $L_{\text{Edd}} = 4\pi GMm_p c/\sigma_T = 1.26 \times 10^{46} (M/10^8 M_\odot) \text{ erg s}^{-1}$, m_p is the proton mass and σ_T is the Thomson cross section. The fiducial disk structure adopts Sirko & Goodman (2003) model with parameters $M = 10^8 M_\odot$, $\dot{M} = 0.1 \dot{M}_{\text{Edd}}$, $\alpha = 0.1$, and opacity $\kappa = 0.34 \text{ cm}^2 \text{ g}^{-1}$. Different disk parameters are shown in the legend, where κ_{disk} represents the opacity as a function of density and temperature which is set as an approximate form shown in Yang et al. (2019); TQM denotes that the Thompson et al. (2005) disk model is adopted.

where the disk surface z_{edge} is set as H_d , $\sqrt{6}H_d$, and infinity for the uniform disk, polytropic disk, and isothermal disk, respectively. As shown in Figure 1, the inner region of the AGN disk is extremely optically thick with $\tau_d(z=0) \gg 1$, and the photosphere location is close to the disk surface. Both polytropic and isothermal disk exhibit a higher photosphere due to their more extended gas distribution, yet they maintain a similar total optical depth to the uniform profile because the density remains low beyond H_d .

Since we investigate the thermal emissions from an initially opaque jet system, and various astrophysical events that generate jets typically occur in the inner region of the AGN disk, such as binary stellar-mass black hole mergers (Yang et al. 2019; Tagawa et al. 2020; McKernan et al. 2020a; Rowan et al. 2024; Xue et al. 2025), black hole-neutron star or binary neutron star mergers (McKernan et al. 2020b; Perna et al. 2021b), and stellar-mass black hole hyper-Eddington accretion (Tagawa et al. 2023a), we focus on disk regions where $R \leq 10^5 R_g$. The Sirko & Goodman (2003) model is employed, which well describes these regions, and we set disk parameters as $\alpha = 0.1$ and $\dot{M} = 0.1 \dot{M}_{\text{Edd}}$ below.

2.2. Jet Dynamics

Launched from the central engine and propagating within the AGN disk, a jet interacts with its dense ambient gas at its head. The extremely optically thick environment inhibits photon escape, causing the shocked disk material and jet material to flow laterally from the jet-head and form a pressurized cocoon that envelops the jet body. A schematic diagram is depicted in Figure 2. The structure and evolution of the jet-cocoon system have been extensively investigated in the literature (e.g. Begelman & Cioffi 1989; Matzner 2003; Bromberg et al. 2011; Harrison et al. 2018; Gottlieb et al. 2020, 2021; Hamidani & Ioka 2021; Urrutia et al. 2023; Suzuki et al. 2024), with studies demonstrating that self-consistent analytic models are in good agreement with numerical simulations (Bromberg et al. 2011). In line with our previous work Chen & Dai (2024), we employ the descriptions in Bromberg et al. (2011) to calculate the jet-cocoon dynamics.

The jet-cocoon system is characterized by three key parameters: the movement distance of the jet head z_h , the internal energy stored in the cocoon E_c , and the lateral radius of the cocoon r_c , which evolve over time as

$$\frac{dz_h}{dt} = \beta_h c, \quad (4)$$

$$\frac{dE_c}{dt} = \eta_h L_j (1 - \beta_h), \quad (5)$$

$$\frac{dr_c}{dt} = \beta_c c, \quad (6)$$

where L_j is the jet power. The jet-head velocity is determined by the ram pressure balance between jet and disk medium (Matzner 2003), which can be approximated as

$$\beta_h = \frac{\beta_j}{1 + \tilde{L}^{-\frac{1}{2}}}, \quad (7)$$

where $\beta_j \sim 1$ is the jet velocity, and \tilde{L} is a dimensionless parameter

$$\tilde{L} = \frac{L_j}{\Sigma_h \rho(z) c^3}. \quad (8)$$

η_h represents the fraction of energy transferred from the jet head to the cocoon, depending on the causal connection of the shocked material and determined by the Lorentz factor Γ_h and the opening angle θ_h of the jet head, which is

$$\eta_h = \min\left[\frac{2}{\Gamma_h \theta_h}, 1\right]. \quad (9)$$

Squeezed by the highly pressurized cocoon, the jet would be collimated from a conical to a cylindrical structure. The resulting jet cross-section is

$$\Sigma_h = \pi \theta_j^2 \min\left[z_h^2, \frac{3L_j z_h r_c^2}{4cE_c}\right], \quad (10)$$

where θ_j is the initial opening angle of the jet, the two terms represent the undisturbed case and the collimated case, respectively. The lateral expansion velocity of the cocoon can be estimated as $\beta_c = \sqrt{P_c/\bar{\rho}(z_h)c^2}$. Given that the pressure of a radiation-dominated cocoon is $P_c = E_c/3V_c$, and its volume can be approximated as $V_c = \pi z_h r_c^2$, the expression for the velocity becomes

$$\beta_c = \left[\frac{E_c}{3\pi\bar{\rho}(z_h)c^2 z_h r_c^2} \right]^{\frac{1}{2}}, \quad (11)$$

where $\bar{\rho}(z_h)$ is the averaged density of the cocoon at z_h . Combining Equations (4)-(11), the comprehensive dynamical evolution of the jet-cocoon system can be calculated self-consistently. For simplicity, the jet is assumed to be always launched at the mid-plane of AGN disk and propagates perpendicular to the disk plane, with initial parameters $\Gamma_j = 100$ and $\theta_j = 0.17$.

Four illustrative examples for the evolution of a jet-cocoon system are shown in Figure 3. The $L_j = 10^{46}$ erg s⁻¹ case clearly demonstrates the essential characteristics of the jet-cocoon system. The jet is significantly decelerated and collimated during its propagation. Additionally, the vertical motion of the jet-head is much more rapid than the lateral expansion of the cocoon, resulting in an elongated system. When the jet is extremely strong, for instance, with $L_j = 10^{50}$ erg s⁻¹, the ambient gas cannot effectively decelerate the jet, and consequently, the velocity of the jet-head is higher. Despite the significant internal pressure, the cocoon remains too weak to collimate the jet, leading to a nearly constant jet opening angle throughout its propagation. Due to the similarity between ρ_{uni} , ρ_{iso} , and ρ_{poly} within H_d , the dynamics of jet is nearly indistinguishable when its head is deeply embedded within the AGN disk for these three vertical density profile. Since the isothermal and polytropic disk are more extended, the jet would continuously propagate within the AGN disk ahead of H_d . Moreover, as the ambient density decreases sharply, the tenuous gas inefficiently brakes the jet, allowing it to reaccelerate. For the specific GRB jets, Zhang et al. (2024) demonstrated similar dynamical properties of jet propagation to those presented in our study.

2.3. Jet Choking

We define a critical height z_{bre} as the jet shock breakout height, where $\tau_d(z_{\text{bre}}) = 1/\beta_h$. Below z_{bre} , photons are predominantly trapped within the jet-cocoon system because the photon diffusion is slower than the shock propagation, where we simplistically neglect photon leakage from the laterally expanding cocoon. Above z_{bre} , photons can efficiently escape from the shocked jet-head, producing thermal emission and leading to the jet breakout. The width of the shock breakout shell can be estimated as (Chen & Dai 2024)

$$d_{\text{bre}} = \frac{1}{\kappa \rho(z_{\text{bre}}) \beta_h}. \quad (12)$$

As shown in Figure 4 and Table 1, the breakout shell displays an extremely thin structure, indicating that jet breakout occurs close to the disk surface, attributed to the high jet-head velocity and the substantial environmental optical

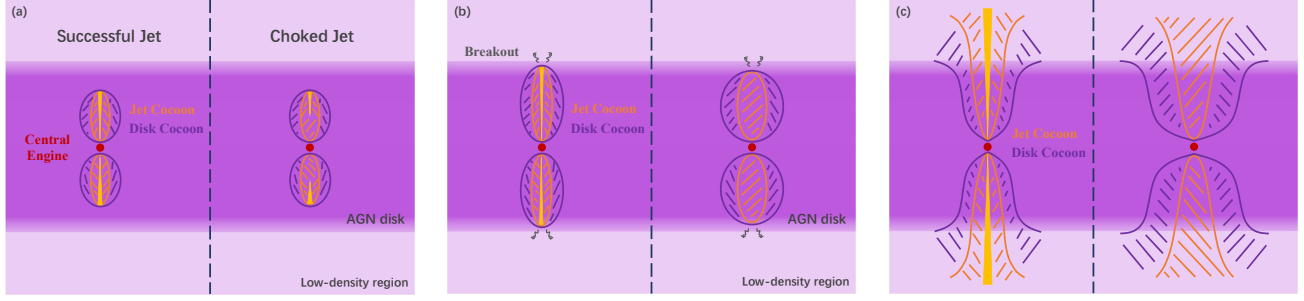


Figure 2. Schematic description of the jet propagation in the AGN disk. (a) Depending on the duration of the central engine, a jet can either successfully penetrate the disk or become choked. Prior to engine cut-off and before the jet’s tail catching up with its head, both successful and choked jet system exhibit similar structure: a jet-body enveloped by a two-component cocoon. (b) For the successful jet, the ram pressure exerted on the jet head facilitates rapid forward propagation, which in turn maintains the slender shape of the jet-cocoon system. In contrast, once the jet is choked and dissipates, the cocoon expands both longitudinally and laterally driven by its internal pressure, resulting in a wider structure. At the breakout, photons can diffuse out from either the jet-head or the cocoon-head to produce emission. (c) No matter whether the jet is choked or not, the two-component cocoon expands ahead of AGN disk and continuously emits thermal radiation.

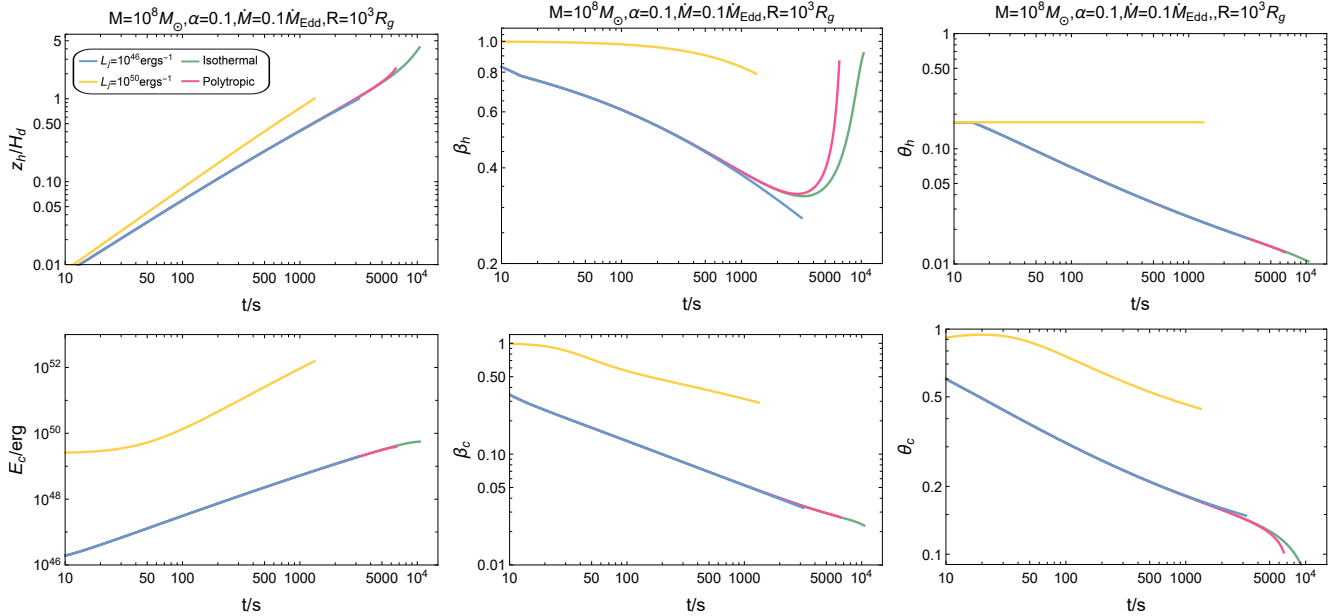


Figure 3. Evolution of system parameters in illustrative jet-cocoon systems. The blue, yellow, green, and magenta lines represent the propagation dynamics of a $10^{46} \text{ erg s}^{-1}$ jet embedded at the mid-plane of an AGN disk with a uniform density profile, as well as jet with higher power of $10^{50} \text{ erg s}^{-1}$ or different density profiles. The endpoint of each line indicates the time of jet breakout.

depth. The jet-head velocity varies significantly as a function of the jet power, ranging from Newtonian to mild-relativistic regimes, which contributes to distinct properties in its shock breakout emission (see below). Given that the jet experiences reacceleration in the isothermal disk, the jet-head velocity at breakout exceeds that in a uniform disk. Correspondingly, the shock breakout time t_{bre} of the jet can be defined as the time required for its head to reach z_{bre} . As shown in Figure 5, a more rapid breakout is observed in the inner region of the AGN disk surrounding less massive SMBH, mainly attributed to the thinner vertically structure of the disk. Meanwhile, a more powerful jet breaks out relatively earlier because it is less prone to deceleration. Additionally, it is evident that a thicker isothermal or polytropic disk results in a later breakout.

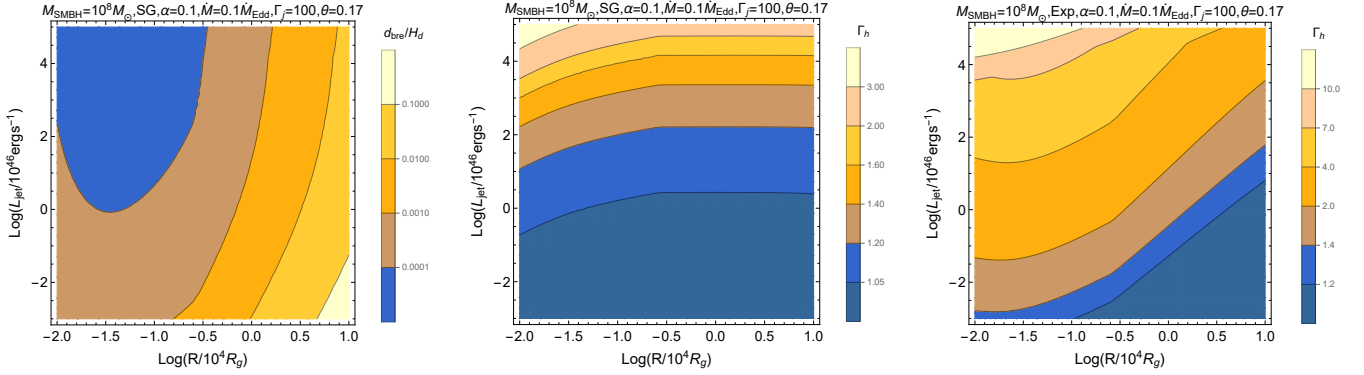


Figure 4. Properties of the jet head at shock breakout. The left and middle panels respectively depict the width of the shock breakout shell (in units of the disk height H_d) and the Lorentz factor of the jet head at breakout, assuming a uniform disk density profile. The right panel shows the Lorentz factor of the jet head at breakout under an isothermal disk density profile.

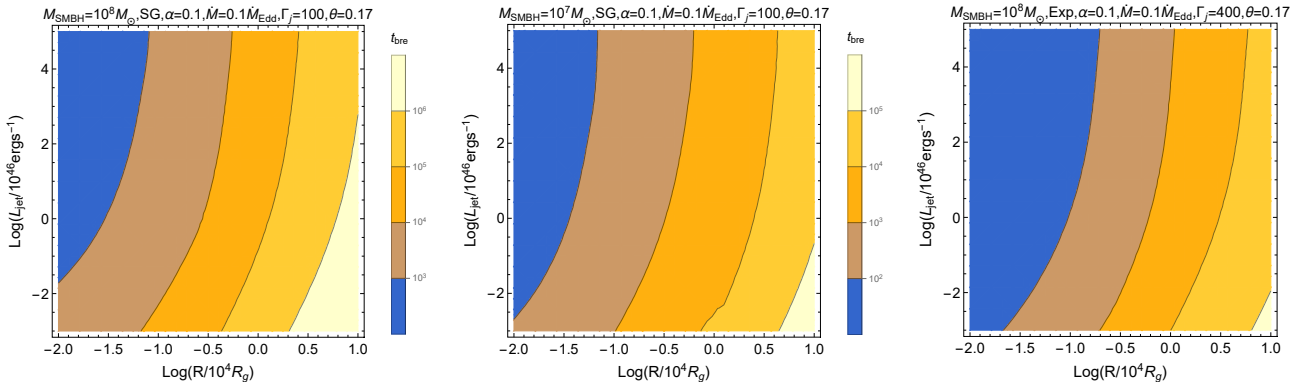


Figure 5. Time for shock breakout of the embedded-jet, assuming its launch at the midplane of AGN disk, in units of s. The parameters are identical to those in Figure 4. In the middle panel, the SMBH mass is set to $M = 10^7 M_\odot$.

Depending on the jet-launching mechanism of the central engine, a powerful jet can remain active for a duration of t_j before being shut off. During propagation through the AGN disk, the jet undergoes deceleration at its head while maintaining ultra-relativistic velocities along its body. After the central engine stops, the last launched tail continues to pursue the jet head until it eventually catches up. If the convergence occurs prior to the jet shock breakout, the jet becomes choked and all of its matter and kinetic energy are transferred into the cocoon (e.g. Irwin et al. 2019; Eisenberg et al. 2022; Pais et al. 2023). Therefore, the jet choking time is given by

$$t_{\text{ch}} = t_j + \int_0^{t_{\text{ch}}} \beta_h dt. \quad (13)$$

If the jet choking time is shorter than the jet breakout time t_{bre} , the jet fails to emerge from the AGN disk, leaving only a cocoon; conversely, the jet successfully breaks out. A critical situation occurs when $t_{\text{ch}} = t_{\text{bre}}$, leading to the derivation of the minimum jet duration time as $t_{j,\text{cri}} = t_{\text{bre}} - z_h(t_{\text{bre}})/c$.

The value of $t_{j,\text{cri}}$ is shown in Figure 6. Similar to the properties of t_{bre} , we find that jets with higher power launched at the inner region of the AGN disk around less massive SMBH are more likely to break out. The extended isothermal or polytropic disk significantly impedes jet propagation, leading to a more delayed breakout and a higher $t_{j,\text{cri}}$. Given the substantial variations in the power, duration, and total energy of jets embedded in AGN disks, such as for GRB jets where the duration ranges from 10^{-2} s to 10^3 s (e.g. Qin et al. 2013) and the total energy primarily spans 10^{48} erg to 10^{53} erg (e.g. Liang et al. 2008; Cenko et al. 2010), while for BBH-merger jets or isolated-accreting-BH jets, the power ranges from 10^{43} erg s $^{-1}$ to 10^{50} erg s $^{-1}$ (e.g. Wang et al. 2021b; Tagawa et al. 2023a,b, 2024; Chen & Dai 2024), with the duration varying on scale of the accretion timescale over a wide range from 10^4 s to 10^7 s (e.g. Tagawa et al.

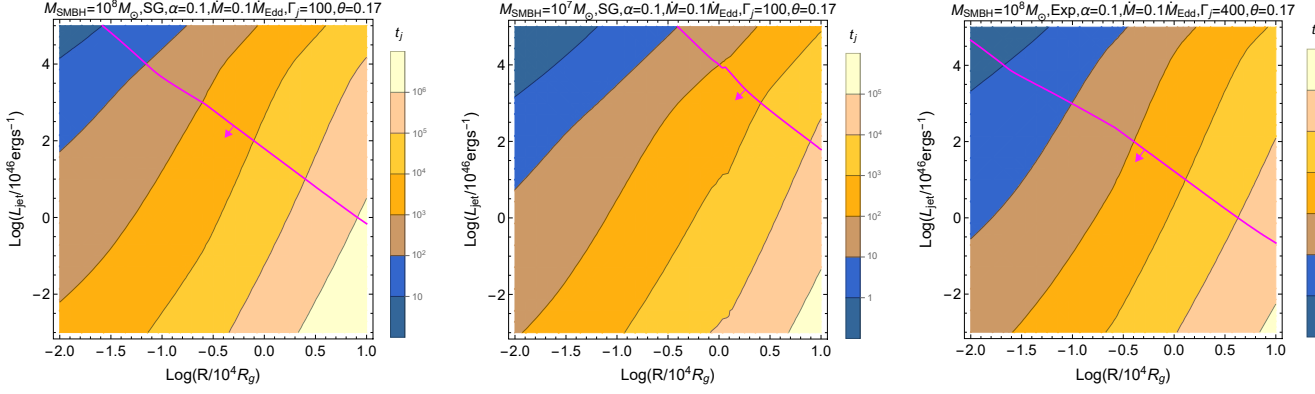


Figure 6. Minimum active duration of the center engine for jet breakout, in units of s. The parameters are identical to those in Figure 5. For a jet with specific power at a given AGN disk location, the left side of the contour represents the choked region. The magenta line and the region to its left indicate that the total energy of the jet is $\leq 10^{52}$ erg.

2022; Chen & Dai 2024; Kim & Most 2024), these jets may either successfully break out of the AGN disks or become choked.

3. THERMAL EMISSION

No matter whether the jet is choked or not, the entire jet-cocoon system remains opaque when embedded within the AGN disk. The shocked regions, specifically the jet head and cocoon, are radiation-mediated where photons and gas are tightly coupled. Consequently, the initial emission from the breakout system appears as thermal radiation. In what follows, we investigate the thermal emission from the jet head, disk cocoon, and jet cocoon when the jet successfully breaks out of the AGN disk, or the thermal emission from the disk and jet cocoon in the case of a choked jet (see Figure 2).

3.1. Jet-head Shock Breakout Emission

The emission properties of a radiation-mediated shock, including luminosity, duration, and temperature, are significantly influenced by both its velocity and the ambient gas density (e.g. Levinson & Nakar 2020). As shown in Figure 4, the velocity of the jet head at shock breakout varies significantly among jets with different power levels originating from various AGN disk locations with distinct gas densities. Consequently, the jet-head shock breakout emission correspondingly exhibits diverse properties. Following Tagawa et al. (2023b) and Chen & Dai (2024), we investigate this emission component.

When the jet head is Newtonian, photons behind the radiation-mediated shock can escape from the breakout shell and carry away its internal energy within the diffusion timescale. According to the shock jump condition (Frank et al. 2002), internal energy constitutes the major portion of the total energy, so it is given by

$$E_{h,bre} \simeq \rho \Sigma_h d_{bre} \beta_h^2 c^2, \quad (14)$$

where all parameter values are evaluated at z_{bre} . Considering the diffusion timescale as the duration of the emission, which can be expressed as

$$t_{diff,h} = \frac{1}{\kappa \rho \beta_h^2 c}, \quad (15)$$

the luminosity of the jet-head shock breakout emission is estimated as

$$L_{h,bre} \simeq \frac{E_{h,bre}}{t_{diff,h}} = \Sigma_h \rho \beta_h^3 c^3. \quad (16)$$

The typical radiation temperature of the breakout shell is determined by its degree of thermalization (e.g. Nakar & Sari 2010). The thermal equilibrium temperature behind the radiation-dominant shock is

$$T_{BB,hbre} = \left(\frac{18}{7a} \rho \beta_h^2 c^2 \right)^{\frac{1}{4}}, \quad (17)$$

where a is the radiation constant. For a sufficiently high-velocity shock, the photons generated through the free-free process are inadequate to share the internal energy effectively. In this scenario, Compton scattering provides additional photon-electron coupling, allowing the breakout shell to approach equilibrium at a temperature larger than $T_{\text{BB,hbre}}$ (Nakar & Sari 2010; Katz et al. 2010). The Comptonization-modified radiation temperature within the range $0.03 < \beta_{\text{h}} < 0.4$ can be calculated using the fitting formulae presented as (Sapir et al. 2013)

$$\log_{10} \left(\frac{T_{\text{Com,hbre}}}{\text{eV}} \right) = 0.975 + 1.735 \left(\frac{\beta_{\text{h}}}{0.1} \right)^{\frac{1}{2}} + \left[0.26 - 0.08 \left(\frac{\beta_{\text{h}}}{0.1} \right)^{\frac{1}{2}} \right] \log_{10} \left(\frac{n}{10^{15} \text{ cm}^{-3}} \right), \quad (18)$$

where $n = \rho/m_{\text{p}}$ is the number density of the AGN disk gas. For $\beta_{\text{h}} < 0.03$, the breakout shell reaches thermal equilibrium, and the radiation temperature is given by Equation (17).

The thermal emission characteristics of a relativistic breakout shell exhibit substantial differences compared to those in the aforementioned Newtonian shocked shell. For $\beta_{\text{h}} > 0.5$, even when accounting for Compton scattering, the shock temperature exceeds 50 keV, leading to the copious production of positron-electron pairs (e.g. Weaver 1976; Svensson 1982). These pairs are the primary sources that generate photons, facilitating the shock downstream to reach equilibrium, and adjust the rest-frame temperature behind a radiation-mediated shock to be nearly constant at ~ 200 keV (e.g. Budnik et al. 2010; Katz et al. 2010). Meanwhile, pairs production substantially increases the leptons number density within the breakout shell, rendering it initially opaque even though the upstream optical depth $\tau_{\text{d}}(z_{\text{bre}}) \leq 1$ (e.g. Budnik et al. 2010; Nakar & Sari 2012). Moreover, after breaking out of the AGN disk, the relativistic shell undergo continuous acceleration driven by its internal energy until either all energy is converted into bulk kinetic energy or the shell becomes transparent (e.g. Tan et al. 2001; Pan & Sari 2006). We follow Nakar & Sari (2012) to model the emission.

The initial internal energy of the breakout shell is

$$E_0 = \gamma_{\text{h}}^2 M_{\text{h}} c^2, \quad (19)$$

where $\gamma_{\text{h}} = \Gamma_{\text{h}}/\sqrt{2}$ is the initial Lorentz factor of the shocked gas, and $M_{\text{h}} = \Sigma_{\text{h}} d_{\text{bre}} \rho \sim \Sigma_{\text{h}}/\kappa$ is the mass of the shell. Considering shell acceleration, pair-production, and adiabatic cooling, photons can diffuse out of the shell at $t_{\text{h,th}}$, by which time the shell has attained $\gamma_{\text{h,th}}$, with the specific expressions detailed in Appendix A. The emission energy is given by

$$E_{\text{h,bre}}^{\text{R}} = E_0 \frac{\gamma_{\text{h,th}} T'_{\text{th}}}{\gamma_{\text{h}} T_{\text{h}}}, \quad (20)$$

where $T'_{\text{h}} = 200$ keV and $T'_{\text{th}} = 50$ keV are the rest-frame temperatures at shell breakout and when the shell becomes optically thin (Nakar & Sari 2012), respectively. The observed duration of the emission can be estimated as

$$t_{\text{h,bre}}^{\text{obs}} \approx \frac{t_{\text{h,th}}}{2\gamma_{\text{h,th}}^2}, \quad (21)$$

and the resulting luminosity of the jet-head shock breakout emission is

$$L_{\text{h,bre}}^{\text{R}} \simeq \frac{E_{\text{h,bre}}^{\text{R}}}{t_{\text{h,bre}}^{\text{obs}}} = \frac{\gamma_{\text{h,th}}^3}{2\gamma_{\text{h}}} \frac{E_0}{t_{\text{h,th}}}. \quad (22)$$

Considering the beaming effect, the isotropic equivalent luminosity would correspond to an amplification of $L_{\text{h,bre}}^{\text{R}}$ by a factor of $\sim 2\gamma_{\text{h,th}}^2$. For the relativistic shell, the observed temperature of the breakout emission is

$$T_{\text{h,bre}}^{\text{obs}} = T'_{\text{th}} \gamma_{\text{h,th}}. \quad (23)$$

For simplicity, we extrapolate the velocity limit and apply the relativistic shell model for cases where $\beta_{\text{h}} > 0.4$.

3.2. Disk-cocoon Emission

After the jet-head shock breakout, no further energy is injected into the cocoon. Subsequently, the radiation-dominated disk cocoon expands under its inherent pressure. Although overly simplistic, we independently investigate

the evolution of cocoon to obtain a preliminary understanding of its thermal emission properties. The initial parameters of the cocoon are determined by the jet-cocoon dynamics at the jet breakout. We assume half of the cocoon energy is allocated to its disk-component.

Given the longer evolutionary timescale of the disk cocoon compared to the jet-head, we investigate the temporal evolution of luminosity for disk-cocoon emission, assuming that this emission arises subsequent to the jet-head shock breakout. Similar to the jet head, the disk cocoon emits radiation during its shock breakout, with the luminosity and timescale of the emission given by

$$L_{c,\text{bre}} = \pi r_c^2 \rho \beta_c^3 c^3, \quad (24)$$

and

$$t_{c,\text{bre}} = \frac{1}{\kappa \rho \beta_c^2 c}. \quad (25)$$

The luminosity at $t \leq t_{c,\text{bre}}$ is approximated by the leakage of photons from a static slab, characterized by a diffusion time $t_{c,\text{bre}}$ (Nakar & Sari 2010), with the rise in luminosity following $L_c \propto \exp[1 - t_{c,\text{bre}}/t]$; while for $t_{c,\text{bre}} < t \leq t_{c,\text{pla}}$, the breakout shell undergoes adiabatic expansion primarily perpendicular to the disk surface to grow its width in the planar phase, where $t_{c,\text{pla}}$ denotes the transition time between the planar and spherical geometries of the expanding cocoon. The planar geometry dictates the luminosity evolving as $L_c \propto (t/t_{c,\text{bre}})^{-\frac{4}{3}}$ (Nakar & Sari 2010), with the simplification neglecting the light travel effect. For $t > t_{c,\text{pla}}$, the expansion geometry evolves into a nearly spherical configuration with an initial radius $\sim r_c$. The luminosity is modeled as the expansion of an opaque fireball without external power input, starting from $t_{c,\text{pla}}$, in accordance with Equation (3) in Chatzopoulos et al. (2012). At the beginning of spherical phase, the internal energy of the cocoon material escaping the AGN disk is approximate $E_{c,\text{th0}} \sim E_c r_c / 2H_d$, and the initial diffusion timescale is $t_{c,0} = \kappa(r_c/H_d)M_c/bcr_c$, where $M_c = \rho V_c$ is the mass of the disk-cocoon, and $b = 13.8$ (Arnett 1982). The resulting effective diffusion timescale is thus (Chatzopoulos et al. 2012)

$$t_{c,\text{diff}} = \sqrt{t_{c,0} t_{s,0}} = \sqrt{\frac{2}{\pi b} \frac{\kappa M_c}{c H_d}}, \quad (26)$$

where $t_{s,0} = r_c/\beta_c c$. And the initial luminosity in the spherical phase is (Chatzopoulos et al. 2012)

$$L_{c,\text{sph}} = \frac{E_{c,\text{th0}}}{t_{c,0}} = \frac{bcr_c E_c}{2\kappa M_c}. \quad (27)$$

Since the structure of disk-cocoon is cylindrical rather than spherical, and its evolution resembles a bubble rising and expanding on the surface of the AGN disk, the luminosity evolution is unlikely to fully adhere to an isotropic spherical expansion (e.g. Nakar & Piro 2014). Therefore, the actual bolometric light curve should be examined via numerical simulation methods. However, for simplicity, we directly connect the planar and spherical phase at

$$t_{c,\text{pla}} = t_{c,\text{bre}} \left(\frac{L_{c,\text{bre}}}{L_{c,\text{sph}}} \right)^{\frac{3}{4}}. \quad (28)$$

Consequently, the temporal evolution of luminosity for disk-cocoon emission is described by

$$L_c(t) = \begin{cases} L_{c,\text{bre}} \exp \left[1 - \frac{t_{c,\text{bre}}}{t} \right], & t \leq t_{c,\text{bre}} \\ L_{c,\text{bre}} \left(\frac{t}{t_{c,\text{bre}}} \right)^{-\frac{4}{3}}, & t_{c,\text{bre}} < t \leq t_{c,\text{pla}} \\ L_{c,\text{sph}} \exp \left[-\frac{(t-t_{c,\text{pla}})(t+t_{c,\text{pla}})}{2t_{c,\text{diff}}^2} \right], & t > t_{c,\text{pla}} \end{cases} \quad (29)$$

For $\beta_c < 0.03$, the disk-cocoon maintains thermal equilibrium. The temporal evolution of the emission temperature can be derived from the observed effective temperature $T_{\text{BB},c} \propto (L_c/r_{\text{ph}})^{\frac{1}{4}}$ (e.g. Piro et al. 2021), where the photosphere radius r_{ph} remains nearly constant during the breakout and planar phases, whereas $r_{\text{ph}} \simeq \beta_c t$ during the spherical phase. Therefore, the emission temperature evolves as

$$T_{\text{BB},c}(t) \propto \begin{cases} \exp \left[1 - \frac{t_{c,\text{bre}}}{t} \right]^{\frac{1}{4}}, & t \leq t_{c,\text{bre}} \\ \left(\frac{t}{t_{c,\text{bre}}} \right)^{-\frac{1}{3}}, & t_{c,\text{bre}} < t \leq t_{c,\text{pla}} \\ \exp \left[-\frac{(t-t_{c,\text{pla}})(t+t_{c,\text{pla}})}{2t_{c,\text{diff}}^2} \right]^{\frac{1}{4}} \left(\frac{t}{t_{c,\text{pla}}} \right)^{-\frac{1}{2}}, & t > t_{c,\text{pla}} \end{cases} \quad (30)$$

where $T_{\text{BB},c}(t_{c,\text{bre}}) = T_{\text{BB},c\text{bre}} = (18\rho\beta_c^2 c^2/7a)^{\frac{1}{4}}$.

When $\beta_c > 0.03$, the emission temperature is initially out of thermal equilibrium, leading to a more complex evolution process. The degree of thermalization can be reflected by a coefficient $\eta \equiv n_{\text{BB}}/t_{\text{cp}}\dot{n}_{\text{ph,ff}}$ (Nakar & Sari 2010), where $n_{\text{BB}} \sim aT_{\text{BB}}^4/3kT_{\text{BB}}$ is the photon number density required for thermal equilibrium, k is the Boltzmann constant, $\dot{n}_{\text{ph,ff}} \approx 3.5 \times 10^{36} \text{ s}^{-1} \text{ cm}^{-3} \rho^2 T^{-\frac{1}{2}}$ is the photon production rate via free-free process, and t_{cp} is the time over which photons can couple with the gas. For $\eta > 1$, the Comptonization-modified temperature is given by $T_{\text{Com},c} = T_{\text{BB},c}\eta(T_{\text{BB},c})^2/\xi(T_{\text{Com},c})^2$ (Nakar & Sari 2010), where ξ is the Comptonization correction factor. Neglecting the evolution of ξ , an approximate relation $T_{\text{Com},c} \propto T_{\text{BB}}\eta^2$ is derived. During the breakout phase, accounting for photon leakage from a static slab (Nakar & Sari 2010), the optical depth of the breakout shell $\tau \propto t$, the thermal equilibrium temperature $T_{\text{BB}} \propto L_c\tau$, and $t_{\text{cp}} \propto t^2$, resulting in $\eta \propto \exp[1 - t_{c,\text{bre}}/t]^{\frac{7}{8}} t^{-\frac{9}{8}}$, and thereby $T_{\text{Com},c} \propto \exp[1 - t_{c,\text{bre}}/t]^2 (t/t_{c,\text{bre}})^{-2}$. Similarly, during the planar phase, the observed temperature evolves as $T_{\text{Com},c} \propto (t/t_{c,\text{bre}})^{-\frac{2}{3}}$ (Nakar & Sari 2010). In the early stage of spherical phase, the increase in η leads to inefficient photon production. The temperature thus evolves following adiabatic cooling, $T_{\text{Com},c} \propto (\beta_c^3 t^3)^{-\frac{1}{3}}$, until at $t_{c,\text{th}}$, the expanding disk-cocoon re-establishes thermal equilibrium with $T_{\text{Com},c} = (L_c/4\pi r_{\text{ph}}^2 \sigma_{\text{SB}})^{\frac{1}{4}}$, where σ_{SB} is the Stefan–Boltzmann constant. Combining all phases, the emission temperature can be approximately described as

$$T_{\text{Com},c}(t) \propto \begin{cases} \exp\left[1 - \frac{t_{c,\text{bre}}}{t}\right]^2 \left(\frac{t}{t_{c,\text{bre}}}\right)^{-2}, & t \leq t_{c,\text{bre}} \\ \left(\frac{t}{t_{c,\text{bre}}}\right)^{-\frac{2}{3}}, & t_{c,\text{bre}} < t \leq t_{c,\text{pla}} \\ \left(\frac{t}{t_{c,\text{pla}}}\right)^{-1}, & t_{c,\text{pla}} < t \leq t_{c,\text{th}} \\ \exp\left[-\frac{(t-t_{c,\text{th}})(t+t_{c,\text{th}})}{2t_{c,\text{diff}}^2}\right]^{\frac{1}{4}} \left(\frac{t}{t_{c,\text{th}}}\right)^{-\frac{1}{2}}, & t > t_{c,\text{th}} \end{cases} \quad (31)$$

where $T_{\text{Com},c}(t_{c,\text{bre}}) = T_{\text{Com},c\text{bre}}$, which is calculated via substituting β_c in Equation (18) to replace β_h . Furthermore, during the planar phase, the photon-gas thermal coupling increases over time as $\eta \propto t^{-\frac{1}{6}}$ (Nakar & Sari 2010). Consequently, the breakout shell may attain thermal equilibrium when $\eta = 1$ at $t_{c,\text{thp}} = \eta(t_{c,\text{bre}})^6 t_{c,\text{bre}}$ in the planar phase. If $t_{c,\text{thp}} < t_{c,\text{pla}}$, the emission temperature evolves as

$$T_{\text{Com},c}(t) \propto \begin{cases} \exp\left[1 - \frac{t_{c,\text{bre}}}{t}\right]^2 \left(\frac{t}{t_{c,\text{bre}}}\right)^{-2}, & t \leq t_{c,\text{bre}} \\ \left(\frac{t}{t_{c,\text{bre}}}\right)^{-\frac{2}{3}}, & t_{c,\text{bre}} < t \leq t_{c,\text{thp}} \\ \left(\frac{t}{t_{c,\text{thp}}}\right)^{-\frac{1}{3}}, & t_{c,\text{thp}} < t \leq t_{c,\text{pla}} \\ \exp\left[-\frac{(t-t_{c,\text{pla}})(t+t_{c,\text{pla}})}{2t_{c,\text{diff}}^2}\right]^{\frac{1}{4}} \left(\frac{t}{t_{c,\text{pla}}}\right)^{-\frac{1}{2}}, & t > t_{c,\text{pla}} \end{cases} \quad (32)$$

Next, we investigate the luminosity and temperature evolution of the disk-cocoon emission in the stratified disk. As shown in Figure 3, the disk cocoon undergoes continuous deceleration because, according to Equation (11), $\beta_c \propto \bar{\rho}(z_h)^{-\frac{1}{2}}$, where the vertical averaged density of both isothermal and polytropic disk is determined by the heavy material within H_d and decreases slowly. Although employing the averaged density provides a more precise description on jet collimation and the general dynamical evolution of the jet-cocoon system, it significantly overestimates the local density at heights exceeding H_d , which determines the instantaneous velocity of the cocoon. As a result, the sharp drop in density above H_d in an isothermal or polytropic disk results in the acceleration of the uppermost portion of the disk cocoon material. This acceleration induces additional evolution of luminosity and temperature in the early stages following breakout (e.g. Nakar & Sari 2010; Piro et al. 2021). Detailed properties of this disk-cocoon emission are provided in Appendix B.

3.3. Jet-cocoon Emission

We follow Nakar & Piran (2017) to investigate the jet-cocoon emission. During the jet propagation within the AGN disk, the less-dense jet-cocoon would undergo mixing with the disk-cocoon via instabilities (e.g. Morsony et al. 2007; Gottlieb et al. 2020, 2021), despite the radiation-dominated pressure (energy density) being equal (Bromberg et al.

2011). Depending on the interaction duration, shocked jet materials at different heights hold varying mixing level, and thereby jet-cocoon becomes stratified, with material near the base of jet showing greater mixing and higher density, while material closer to the jet head experiences less mixing and lower density (Eisenberg et al. 2022). Moreover, mixing results in an approximately uniform distribution of jet-cocoon energy on a logarithmic scale of energy per baryon, primarily in the form of internal energy (Gottlieb et al. 2020, 2021). Consequently, the fraction of jet-cocoon energy deposited in material with a specific terminal proper velocity $\Gamma_{\text{cj}}\beta_{\text{cj}}$, after internal energy primarily converted into kinetic energy, can be assumed to a constant $f_{\Gamma\beta}$, denoted as $f_{\Gamma\beta} \sim 0.1$ (Nakar & Piran 2017).

For the Newtonian jet-cocoon material with a terminal velocity $\beta_{\text{cj}} \lesssim 0.7$, its mass is estimated as

$$m_{\text{cj},\beta} \simeq \frac{2f_{\Gamma\beta}E_{\text{cj}}}{\beta_{\text{cj}}^2 c^2}, \quad (33)$$

where $E_{\text{cj}} \simeq E_c/2$ is the total energy of the jet-cocoon, and its initial volume can be approximated by

$$V_{\text{cj},\beta} \simeq f_{\Gamma\beta} \pi r_c^2 z_{\text{bre}}. \quad (34)$$

After adiabatic expansion, photons can diffuse out of the jet-cocoon shell, referred to as the luminosity shell (Nakar & Sari 2010), to generate emission when $\kappa m_{\text{cj},\beta}/4\pi r_{\text{cj}}^2 = 1/\beta_{\text{cj}}$ is satisfied, thus the diffusion radius is given by

$$r_{\text{cj}} = \left(\frac{\kappa f_{\Gamma\beta} E_{\text{cj}}}{2\pi \beta_{\text{cj}} c^2} \right)^{\frac{1}{2}}, \quad (35)$$

and the corresponding diffusion time is

$$t_{\text{cj}} \simeq \left(\frac{\kappa f_{\Gamma\beta} E_{\text{cj}}}{2\pi \beta_{\text{cj}}^3 c^4} \right)^{\frac{1}{2}}. \quad (36)$$

The resulting emission luminosity is estimated as

$$L_{\text{cj}} = \frac{f_{\Gamma\beta} E_{\text{cj}}}{t_{\text{cj}}} \frac{V_{\text{cj},\beta}^{\frac{1}{3}}}{r_{\text{cj}}} = \frac{2\pi \beta_{\text{cj}}^2 c^3 V_{\text{cj},\beta}^{\frac{1}{3}}}{\kappa}. \quad (37)$$

We set $\beta_{\text{cj},s} = \min[0.7, \beta_{\text{cr}}]$ as the velocity of the first shell that produces diffusing thermal emission, where $\beta_{\text{cr}} = \kappa f_{\Gamma\beta} E_{\text{cj}}/2\pi r_c^2 c^2$ represents the critical velocity at which $r_{\text{cj}} = r_c$, signifying that photons escape from the jet-cocoon just after the jet breakout (Chen & Dai 2024). Based on the energy distribution $dE/d \log \beta_{\text{cj}} = f_{\Gamma\beta} E_{\text{cj}}$, the mass distribution can be described as $m(> v) \propto v^{-(s+1)}$, where $s \simeq 1$ (Nakar & Piran 2017). Therefore, the properties of luminosity shell evolve over time as $m_{\text{cj}} \propto t^{\frac{2(s+1)}{s+2}}$, $\beta_{\text{cj}} \propto t^{-\frac{2}{s+2}}$, $r_{\text{cj}} \propto t^{\frac{s}{s+2}}$, and $\tau_{\text{cj}} \propto t^{\frac{2}{s+2}}$. As the emission luminosity $L_{\text{cj}} \propto \beta_{\text{cj}}^2$, it evolves as

$$L_{\text{cj}}(t) = L_{\text{cj},s} \begin{cases} \left(\frac{t}{t_{\text{cj},s}} \right)^{-\frac{4}{s+2}}, & t_{\text{cj},s} < t \leq t_{\text{sph, end}} \\ \left(\frac{t_{\text{sph, end}}}{t_{\text{cj},s}} \right)^{-\frac{4}{s+2}} \exp \left[-\frac{1}{2} \left(\frac{t^2}{t_{\text{sph, end}}^2} - 1 \right) \right], & t > t_{\text{sph, end}} \end{cases} \quad (38)$$

where $L_{\text{cj},s}$ and $t_{\text{cj},s}$ are calculated at $\beta_{\text{cj},s}$; $t_{\text{sph, end}}$ denotes the time at which the innermost fully mixed jet-cocoon, whose velocity is assumed to be β_c , becomes radiative, i.e., $t_{\text{sph, end}} = t_{\text{cj},s} (\beta_{\text{cj},s}/\beta_c)^{\frac{s+2}{s}}$. At $t > t_{\text{sph, end}}$, the emission luminosity decreases exponentially as the shell undergoes simultaneous radiative cooling and adiabatic expansion (Piro et al. 2021). The temporal evolution of the emission temperature is examined in a manner analogous to that of the disk-cocoon, which is presented in Appendix C.

For relativistic jet-cocoon materials, the properties of emission are determined by a combination of shell acceleration, spreading, and thermalization (Nakar & Piran 2017). In the dilute radiation-dominated jet-cocoon material, photons can accelerate baryons to a critical Lorentz factor before decoupling, which is given by (Nakar et al. 2005; Nakar & Piran 2017)

$$\gamma_b = \left(\frac{E_{\text{cj}} \sigma_{\Gamma}}{4\pi z_{\text{bre}}^2 \theta_{\text{cj}}^2 \theta_c m_p c^2} \right)^{\frac{1}{4}} = 5.5 E_{\text{cj},50}^{\frac{1}{4}} z_{\text{bre},13}^{-\frac{1}{2}} \theta_{\text{cj}}^{-\frac{1}{2}} \theta_c^{-\frac{1}{4}}, \quad (39)$$

where the numbers in subscripts represent the power of 10, e.g., $E_{\text{cj},50} = E_{\text{cj}}/10^{50}$ erg; and $\theta_c = r_c/z_{\text{bre}}$, $\theta_{\text{cj}} \simeq 0.5$ are the initial and final opening angle of the expanding relativistic jet-cocoon. Another critical Lorentz factor that describes the spreading status of the jet-cocoon material is given by (Nakar et al. 2005; Nakar & Piran 2017)

$$\gamma_s = \left(\frac{E_{\text{cj}} \sigma_{\Gamma}}{4\pi f_{\Gamma\beta} z_{\text{bre}}^2 \theta_{\text{cj}}^2 m_{\text{p}} c^2} \right)^{\frac{1}{5}} = 4.9 E_{\text{cj},50}^{\frac{1}{5}} z_{\text{bre},13}^{-\frac{2}{5}} f_{\Gamma\beta,-1}^{-\frac{1}{5}} \theta_{\text{cj}}^{-\frac{2}{5}}, \quad (40)$$

for gas with $\gamma < \gamma_s$, photons decouple from it when its width is spreading, while for gas with $\gamma > \gamma_s$, photon decoupling occurs prior to the onset of spreading. Furthermore, by setting the thermal coupling coefficient $\eta = 1$, where $T_{\text{BB,cj0}} = (f_{\Gamma\beta} E_{\text{cj}}/a V_{\text{cj},\beta})^{\frac{1}{4}}$, $\rho_{\text{cj},\gamma} = f_{\Gamma\beta} E_{\text{cj}}/\gamma c^2 V_{\text{cj},\beta}$, $t_{\text{cp}} \simeq f_{\Gamma\beta} z_{\text{bre}}/c$, the resulting coefficient is

$$\eta(\gamma) = 1.7 \times 10^4 E_{\text{cj},50}^{-\frac{9}{8}} z_{\text{bre},13}^{\frac{19}{8}} f_{\Gamma\beta,-1}^{-1} \theta_c^{\frac{9}{4}} \gamma^2, \quad (41)$$

and the thermal critical Lorentz factor can be expressed as

$$\gamma_{\text{BB}} = 0.007 E_{\text{cj},50}^{\frac{9}{16}} z_{\text{bre},13}^{-\frac{19}{16}} f_{\Gamma\beta,-1}^{\frac{1}{2}} \theta_c^{-\frac{9}{8}}, \quad (42)$$

gas with $\gamma < \gamma_{\text{BB}}$ can reach thermal equilibrium before generating emission.

In the case of $\gamma_b \lesssim 1.4$, photons decouple from the rarefied gas before accelerating it to relativistic velocity, leading to most of the internal energy being carried away by radiation. Therefore, the duration of the emission is estimated as (Nakar & Piran 2017)

$$t_{\text{cj}} \simeq \frac{f_{\Gamma\beta} z_{\text{bre}}}{c}, \quad (43)$$

and its isotropic equivalent luminosity is

$$L_{\text{cj}} \simeq \frac{E_{\text{cj}} c}{z_{\text{bre}} \theta_{\text{cj}}^2}, \quad (44)$$

where it is assumed that the photons within jet-cocoon materials close to the jet head can escape, while those in the Newtonian jet-cocoon materials remain trapped. Meanwhile, $\gamma_{\text{BB}} \ll 1$ indicates that radiation is far from thermal equilibrium. Regulated by electron-positron pairs, the observed temperature is approximately $T_{\text{cj}} \simeq 200$ keV.

When $\gamma_b > 1.4$, photons can effectively accelerate the gas to a terminal Lorentz factor provided that $\gamma < \gamma_b$. After acceleration, photon-gas decoupling occurs at the photosphere radius

$$R_{\gamma,\text{ph}} = \left(\frac{\kappa f_{\Gamma\beta} E_{\text{cj}}}{2\pi \theta_{\text{cj}}^2 c^2 \gamma} \right)^{\frac{1}{2}}, \quad (45)$$

and thereby the observed duration is

$$t_{\text{cj},\gamma} = \frac{R_{\gamma,\text{ph}}}{2c\gamma^2} = 7.5 \text{ s } E_{\text{cj},50}^{\frac{1}{2}} f_{\Gamma\beta,-1}^{-\frac{1}{2}} \theta_{\text{cj}}^{-1} \gamma_1^{-\frac{5}{2}}. \quad (46)$$

Given that $t_{\text{cj},\gamma}$ for gas with large γ is relatively short, we focus on the gas with $\gamma \leq 10$ when $\gamma_b > 10$. Additionally, since γ_s is generally slightly smaller than γ_b across extensive parameter regions, we restrict our consideration of the maximum gas Lorentz factor to

$$\gamma_{\text{max}} = \min[\gamma_s, 10], \quad (47)$$

and set the minimum gas Lorentz factor as $\gamma_{\text{min}} = 3$. When reaching the photosphere radius, the comoving volume of the luminosity shell with Lorentz factor γ expands to $V'_{\text{ph},\gamma} \sim 2\pi \theta_{\text{cj}}^2 R_{\gamma,\text{ph}}^3/\gamma$. Due to adiabatic cooling, the isotropic equivalent luminosity is estimated as

$$L_{\text{cj}} = \frac{f_{\Gamma\beta} E_{\text{cj}}}{t_{\text{cj},\gamma} \theta_{\text{cj}}^2} \left(\frac{f_{\Gamma\beta} V_c}{V'_{\text{ph},\gamma}} \right)^{\frac{1}{3}} \gamma, \quad (48)$$

which evolves over time as $L_{\text{cj}} \propto t^{-\frac{26}{15}}$, because of the Lorentz factor of the luminosity shell following $\gamma \propto t^{-\frac{2}{5}}$.

The observed temperature is determined by γ_{BB} . For $\gamma_{\text{BB}} > \gamma_{\text{max}}$, the relativistic jet-cocoon materials are completely in thermal equilibrium, and the temperature is given by

$$T_{\text{cj,obs}} = T_{\text{cj0}} \left(\frac{f_{\Gamma\beta} V_c}{V'_{\text{ph},\gamma}} \right)^{\frac{1}{3}} \gamma, \quad (49)$$

where $T_{\text{cj0}} = T_{\text{BB,cj0}}$. As $T_{\text{cj,obs}} \propto \gamma^{\frac{11}{6}}$, the observed temperature evolves over time as $T_{\text{cj,obs}} \propto t^{-\frac{11}{15}}$. On the contrary, for $\gamma_{\text{BB}} < 1.4$, throughout the evolution of relativistic jet-cocoon materials, the emission remains out of thermal equilibrium, and the temperature properties can be analyzed similarly to Appendix C. Based on $T_{\text{BB,cj0}}$, $\eta(\gamma_{\text{max}})$, and pair production, the initial temperature can be determined as $T_{\text{cj0}} = \max[T_{\text{Com,cj}}, 200 \text{ keV}]$. If $T_{\text{cj0}} = T_{\text{Com,cj}}$, as $\eta \propto \gamma^2$, the observed temperature evolves as $T_{\text{cj,obs}} \propto \gamma^{\frac{35}{6}} \propto t^{-\frac{7}{3}}$. Otherwise, if $T_{\text{cj0}} = 200 \text{ keV}$, the initial temperature remains constant. When $4f_{\Gamma\beta} V_c < V'_{\text{ph},\gamma}$, photons escape from the photosphere, and $T_{\text{cj,obs}} \propto t^{-\frac{11}{15}}$; conversely, when $4f_{\Gamma\beta} V_c > V'_{\text{ph},\gamma}$, the temperature evolution is initially governed by pairs, such that $T_{\text{cj,obs}} \propto \gamma \propto t^{-\frac{2}{5}}$, before being determined by photosphere. Once the initial temperature decreases below 50 keV and the pairs disappear, the evolution reverts to Comptonization. Additionally, for $\gamma_{\text{min}} < \gamma_{\text{BB}} < \gamma_{\text{max}}$, the evolution of the observed temperature transitions from a state out of thermal equilibrium to one in thermal equilibrium, with the transition occurring at $t_{\text{cj},\gamma}(\gamma_{\text{BB}})$.

3.4. Choked Jet

After choking, the jet ceases to exist, and the jet-cocoon system exclusively transitions to cocoon expansion driven by its internal pressure. The initial height and width of the cocoon at t_{ch} can be determined from the jet-cocoon dynamics, i.e., $z_{\text{h}}(t_{\text{ch}})$ and $r_{\text{c}}(t_{\text{ch}})$. The internal energy of the cocoon is given by $E_{\text{ch}} = L_{\text{j}} t_{\text{j}}$, where the total jet kinetic energy has been injected into the cocoon. Unlike the anisotropic jet-cocoon evolution where $\beta_{\text{h}} \gg \beta_{\text{c}}$, under the nearly uniform pressure approximation (e.g. Bromberg et al. 2011), the cocoon exhibits comparable expansion velocities in both the forward and lateral directions, as well as similar expansion scales in these directions (Irwin et al. 2019). Therefore, the height, width and velocity of the remaining cocoon produced by the choked-jet at its shock breakout are estimated as

$$\tau_{\text{d}}(z_{\text{ch,bre}}) = 1/\beta_{\text{ch,bre}}, \quad (50)$$

$$r_{\text{ch,bre}} = r_{\text{c}}(t_{\text{ch}}) + z_{\text{ch,bre}} - z_{\text{h}}(t_{\text{ch}}), \quad (51)$$

and

$$\beta_{\text{ch,bre}} = \left(\frac{2E_{\text{ch}}}{M_{\text{ch,bre}} c^2} \right)^{\frac{1}{2}}, \quad (52)$$

where $M_{\text{ch,bre}}$ represents the total mass swept by the system since the jet launching, ignoring the negligible mass of jet material, which is given by

$$M_{\text{ch,bre}} = \pi r_{\text{ch,bre}}^2 \int_0^{z_{\text{ch,bre}}} \rho(z') dz'. \quad (53)$$

The emission properties of the choked-jet cocoon can be derived directly in a manner analogous to that described in Section 3.2, by substituting β_{c} , r_{c} , E_{c} , M_{c} with $\beta_{\text{ch,bre}}$, $r_{\text{ch,bre}}$, E_{ch} , $M_{\text{ch,bre}}$, respectively.

In the early stage after the jet being choked, the cocoon is still clearly divided into the disk component and the jet component. During the overall cocoon expansion, the jet-cocoon undergoes both a continuous transfer of its internal energy to the newly shocked ambient disk material and a continuous mixing with the disk cocoon, resulting in the gradual diminishment of the jet-cocoon material (Eisenberg et al. 2022). When the jet is barely choked, the top of jet-cocoon can be accelerated to large velocity after the cocoon breakout; in contrast, when the jet is deeply choked within the AGN disk, the maximum terminal velocity of the jet-cocoon material decreases significantly after the breakout, and in extremely deep choking cases, the jet-cocoon may almost completely disappear (Eisenberg et al. 2022; Pais et al. 2023). To estimate the maximum velocity of the remnant jet-cocoon, we assume that during the cocoon expansion after jet choking, the energy distribution of the jet-cocoon remains $dE/d \log(\gamma_{\text{cj}} \beta_{\text{cj}}) = f_{\Gamma\beta} E_{\text{cj}}$. Furthermore, we consider that the jet-cocoon transfers its energy to the freshly shocked disk materials starting from its upper part with higher terminal velocity. At jet choking, the height of jet-cocoon is $z_{\text{h}}(t_{\text{ch}})$, and its energy is $E_{\text{ch}}/2$. When the cocoon breaks out, the jet-cocoon has swept up disk materials from $z_{\text{h}}(t_{\text{ch}})$ to $z_{\text{ch,bre}}$, resulting in approximately a $[1 - z_{\text{h}}(t_{\text{ch}})/z_{\text{ch,bre}}]$

fraction of the jet-cocoon energy being dissipated. Setting the maximum terminal Lorentz factor of the energy-loss-free jet-cocoon to 10, the residual energy determines the cut-off velocity as follows:

$$\frac{\log(\gamma_{\text{cut}}\beta_{\text{cut}}) - \log \beta_{\text{ch,bre}}}{\log 10 - \log \beta_{\text{ch,bre}}} \simeq \frac{z_{\text{h}}(t_{\text{ch}})}{z_{\text{ch,bre}}}, \quad \gamma_{\text{cut}}\beta_{\text{cut}} = 10^{\frac{z_{\text{h}}(t_{\text{ch}})}{z_{\text{ch,bre}}} \left(1 - \frac{z_{\text{h}}(t_{\text{ch}})}{z_{\text{ch,bre}}}\right)}. \quad (54)$$

After understanding the properties of the remnant jet-cocoon, we can calculate its emission by applying the method detailed in Section 3.3.

4. OBSERVATIONAL PROPERTIES

4.1. Emission evolution

On account of the distinct properties of the jet-head, disk-cocoon, and jet-cocoon at the jet-cocoon system breakout, the thermal emissions they produce exhibit significant differences. Table 1 presents a variety of representative cases regarding the jet launching and propagating in the AGN disk, of which the evolution of the bolometric luminosity and temperature for the corresponding thermal emission is shown in Figures 7 and 8.

For jet-head breakout emission, the thin width $d_{\text{bre}}/H_{\text{d}} \ll 1$ and the high velocity $\beta_{\text{h}} > 0.1$ of the breakout shell lead to a high luminosity of emission yet an extremely short emission duration. Meanwhile, the shell is out of thermal equilibrium, resulting in a high emission temperature in the X-ray band. Note that, for simplicity, we neglect the detailed temporal evolution of the emission in Figures 7 and 8, acknowledging that actually it is a flare that initially rises and subsequently declines. For disk-cocoon emission, the luminosity evolution exhibits a early rapid rise followed by a normal decline, originating from the disk-cocoon shock breakout process, succeeded by a phase of approximate plateau, which results from photons being trapped in the adiabatic expansion materials, and finally a sharp decline as most photons have diffused out. The evolution of the observed temperature is relatively straightforward, showing a rapid rise followed by a shallow decline, with the emission remaining essentially in thermal equilibrium. For jet-cocoon emission, the early constant luminosity and temperature shown in Figures 7 and 8 are artificial, which corresponds to a flare of photons escaping from the inefficiently accelerated dilute material at the top of the jet-cocoon, carrying almost its entire internal energy. The luminosity evolution of the Newtonian jet-cocoon material produced emission shows a normal decline attributed to the distribution of energy, mass, and velocity within the jet-cocoon, followed by a sharp decline as the entire jet-cocoon becomes radiative. The temperature evolution of the emission demonstrates an extremely sharp decline due to the sensitive Comptonized radiation, succeeded by a shallow decline in thermal equilibrium radiation. Note that the emission would transition continuously from the relativistic phase to the Newtonian phase. However, since the transition phase is difficult to calculate precisely (Nakar & Piran 2017), we neglect this phase in our analysis.

Next, we investigate the effects of environmental factors and jet properties on the emissions. Comparing case 1, 2, and 3, the generation time of emission is strongly influenced by the height of AGN disk, which is because the jet-cocoon system must break out of the AGN disk to produce observable emissions. In contrast to other components, the luminosity of Newtonian jet-cocoon emission demonstrates a stronger dependence on the properties of the AGN disk, as in Equation (37), both β_{cj} and $V_{\text{cj},\beta}$ are significantly modulated by variations in disk density and height. For all emission components, the earlier they are produced, the higher their peak observed temperature, unless pair production suppresses the temperature at approximately 50 keV for the early Newtonian jet-cocoon component emission. As demonstrated by cases 1, 4 and 5, an increase in jet power results in an earlier breakout, characterized by a faster jet-head and cocoon. Consequently, emissions are generated earlier, with all emission components becoming more powerful and achieving higher temperatures. Furthermore, distinct disk vertical density profiles and disk models can substantially influence the emission properties even for the same jet. In cases 6 and 7, the reacceleration of the jet-head leads to a brighter shock breakout emission with higher observed temperature and longer duration. The emission properties of the jet-cocoon remain largely unchanged. Conversely, due to having swept up more disk gas, the disk-cocoon becomes radiative later, both its emission luminosity and peak temperature are slightly lower compared to those of a more compact uniform disk; these similar properties are also manifested in supernova explosions in AGN disks (Grishin et al. 2021). In case 8, the disk adopts the model described in Thompson et al. (2005), representing a lower-density disk. Consequently, the jet-cocoon becomes sufficiently dilute, enabling photons to escape from the entire structure and thereby producing emission immediately following the system breakout, which results in the absence of relativistic or Newtonian jet-cocoon emission. Moreover, the low density of the disk-cocoon, combined with its high expansion velocity, causes a relatively rapid luminosity evolution and a higher peak observed temperature.

Table 1. Cases of jet launching and propagating in the AGN disk. M_{SMBH} (in M_{\odot}) is the mass of the central SMBH; R_j (in R_g) is the jet location in the AGN disk; ρ_0 (in g cm^{-3}) and H_d (in cm) are the mid-plane density and half-thickness of the AGN disk; ρ_z represents the disk vertical density profile (Uni for uniform, Iso for isothermal, and Poly for polytropic) and disk model (TQM for Thompson et al. (2005) model); L_j (in ergs^{-1}) is the jet power, where all the jets are set to be continuous. The properties of the jet-cocoon system at its breakout are given: t_{bre} (in s) is the breakout time starting from the jet launching, d_{bre} (in H_d) is the width of the breakout shell, β_h and β_c are the velocities of the jet-head and the disk-cocoon, θ_h and θ_c are the opening angle of the jet-head and the disk-cocoon.

case	M_{SMBH}	R_j	ρ_0	H_d	ρ_z	L_j	t_{bre}	d_{bre}	β_h	β_c	θ_h	θ_c
1	10^7	10^4	4.1×10^{-10}	4.3×10^{13}	Uni	10^{46}	3.2×10^3	4.7×10^{-4}	0.35	0.046	0.023	0.17
2	10^7	10^3	1.3×10^{-8}	4.3×10^{12}	Uni	10^{46}	272.6	1.2×10^{-4}	0.42	0.062	0.031	0.20
3	10^8	10^4	9.8×10^{-12}	7.0×10^{14}	Uni	10^{46}	6.8×10^4	1.7×10^{-3}	0.25	0.029	0.015	0.14
4	10^7	10^4	4.1×10^{-10}	4.3×10^{13}	Uni	10^{48}	2.0×10^3	2.6×10^{-4}	0.63	0.14	0.072	0.31
5	10^7	10^4	4.1×10^{-10}	4.3×10^{13}	Uni	$L_{b,\text{AGN}}$	4.5×10^3	6.9×10^{-4}	0.24	0.027	0.014	0.14
6	10^7	10^4	4.1×10^{-10}	4.3×10^{13}	Iso	10^{46}	1.0×10^4	7.7×10^{-3}	0.89	0.032	0.015	0.10
7	10^7	10^4	4.1×10^{-10}	4.3×10^{13}	Poly	10^{46}	6.6×10^3	8.2×10^{-2}	0.83	0.038	0.017	0.12
8	10^7	10^4	1.2×10^{-11}	1.7×10^{13}	TQM	10^{46}	752.0	2.1×10^{-2}	0.67	0.17	0.089	0.34

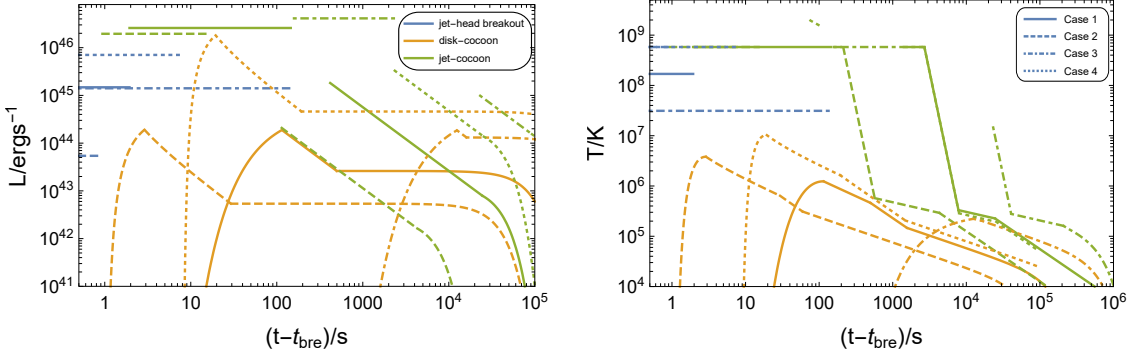


Figure 7. The evolution of bolometric luminosity and temperature for thermal emissions in cases 1, 2, 3, and 4, varying SMBH mass, jet location, and jet power. For thermal emissions, the contributions from the jet-head breakout component, the disk-cocoon component, and the jet-cocoon component are presented separately.

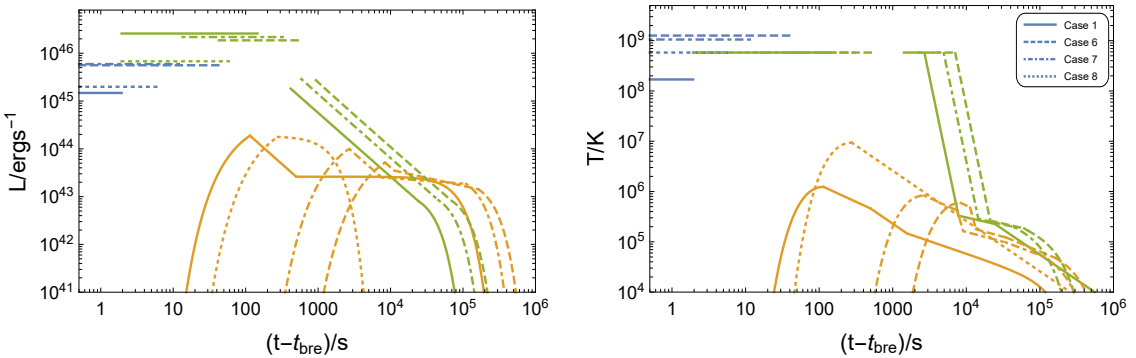


Figure 8. Same as Figure 7, but illustrating different cases featuring various disk vertical density profiles and disk models.

4.2. Detectability

We now investigate the detectability of these thermal emissions, with particular emphasis on the soft X-ray (1 keV), UV (10 eV), and optical (g-band) bands. If brighter than the AGN background radiation, the soft X-ray flare can

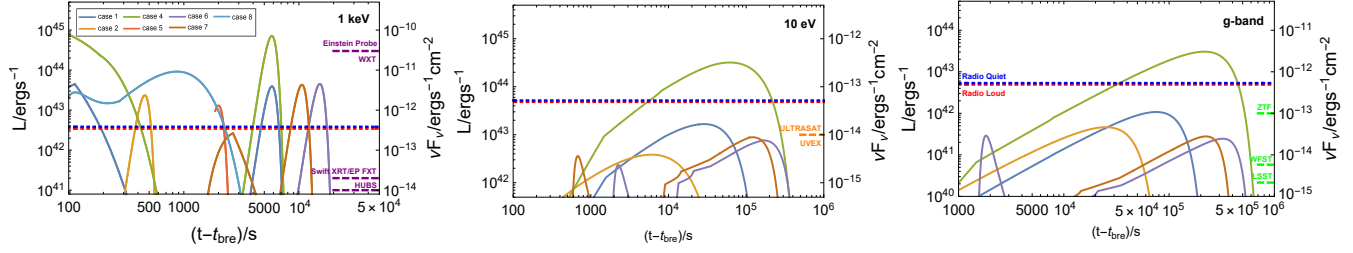


Figure 9. Light curves in soft X-ray (1 keV), UV (10 eV), and optical (g-band) band for various cases. The red and blue dotted lines in each panel represent the typical luminosity of radio-loud and radio-quiet AGN with $M_{\text{SMBH}} = 10^7 M_{\odot}$ in these bands, which are calculated by adopting the mean spectral energy distribution of quasars (Shang et al. 2011). To test detectability, the left and right panels assume a source luminosity distance of $d_L = 300$ Mpc, while the middle panel assumes $d_L = 3$ Gpc. The dashed purple lines mark the sensitivity limit of EP WXT for 1 ks exposure time, Swift XRT, EP FXT, and HUBS for 10 ks exposure time (note that the sensitivity limits of Chandra and XMM-Newton are $\sim 10^{-15}$ ergs $^{-1}$ cm $^{-2}$ for 10 ks exposure time, below the lowest vertical value of the left panel); the dashed orange lines indicate the sensitivity limit of ULTRASAT and UVEX for ~ 1 ks exposure time; the green lines denote the sensitivity limit of ZTF, WFST, and LSST for 30 s exposure time.

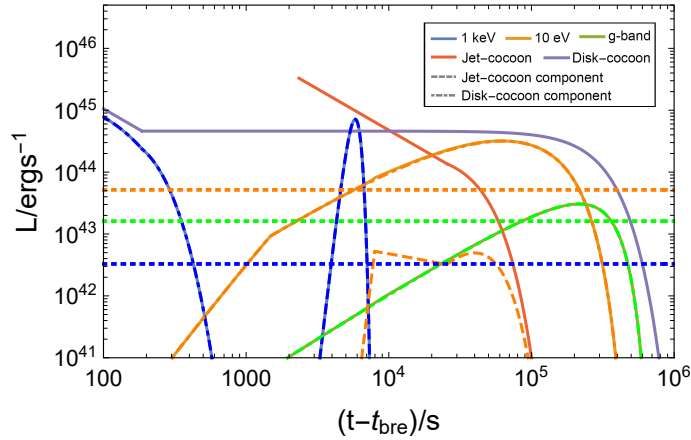


Figure 10. Disk-cocoon and jet-cocoon contributions to the specific-band radiation in case 4. The purple and orange lines represent the bolometric luminosity of the disk-cocoon emission and jet-cocoon emission, respectively. The blue, golden, and green lines depict the overall light curves for X-ray, UV, and optical band, superimposed by the disk-cocoon component shown as a dot-dash line and the jet-cocoon component as a dashed line. Additionally, the blue, orange, and green dotted lines illustrate the radiation of the background AGN.

be captured by telescopes such as Chandra (Weisskopf et al. 2000), XMM-Newton (Jansen et al. 2001), Swift XRT (Burrows et al. 2005), Einstein Probe (EP) (Yuan et al. 2022), and HUBS (Zhang et al. 2022); the UV flare can be observed by facilities like ULTRASAT (Sagiv et al. 2014), and UVEX (Kulkarni et al. 2021); the optical can be detected by telescopes such as LSST (LSST Science Collaboration et al. 2009), ZTF (Bellm 2014), and WFST (Lei et al. 2023).

4.2.1. Soft X-ray

Light curves in the soft X-ray band for various cases are presented in Figure 9. As the AGN background radiation in this band is relatively weak, the X-ray flares produced by jet-cocoon systems are distinguishable in these cases. The elevated luminosity enhances the observed flux surpassing the sensitivity thresholds of various soft X-ray telescopes (as exemplified in the left panel of Figure 9), thus enabling the detection of the flare. Many flares exhibit a profile that rises rapidly and then declines sharply, originating from the Newtonian jet-cocoon component as illustrated in Figure 10. Since these temperatures follow the same Compton evolution, the profiles of the flares are homologous. Meanwhile, in the early stage of cases 1, 4, (7) and 8, additional short-duration flares are observed, which are produced by the fast disk-cocoon component as illustrated in Figure 10. Consequently, some soft X-ray flares displays a double-peak

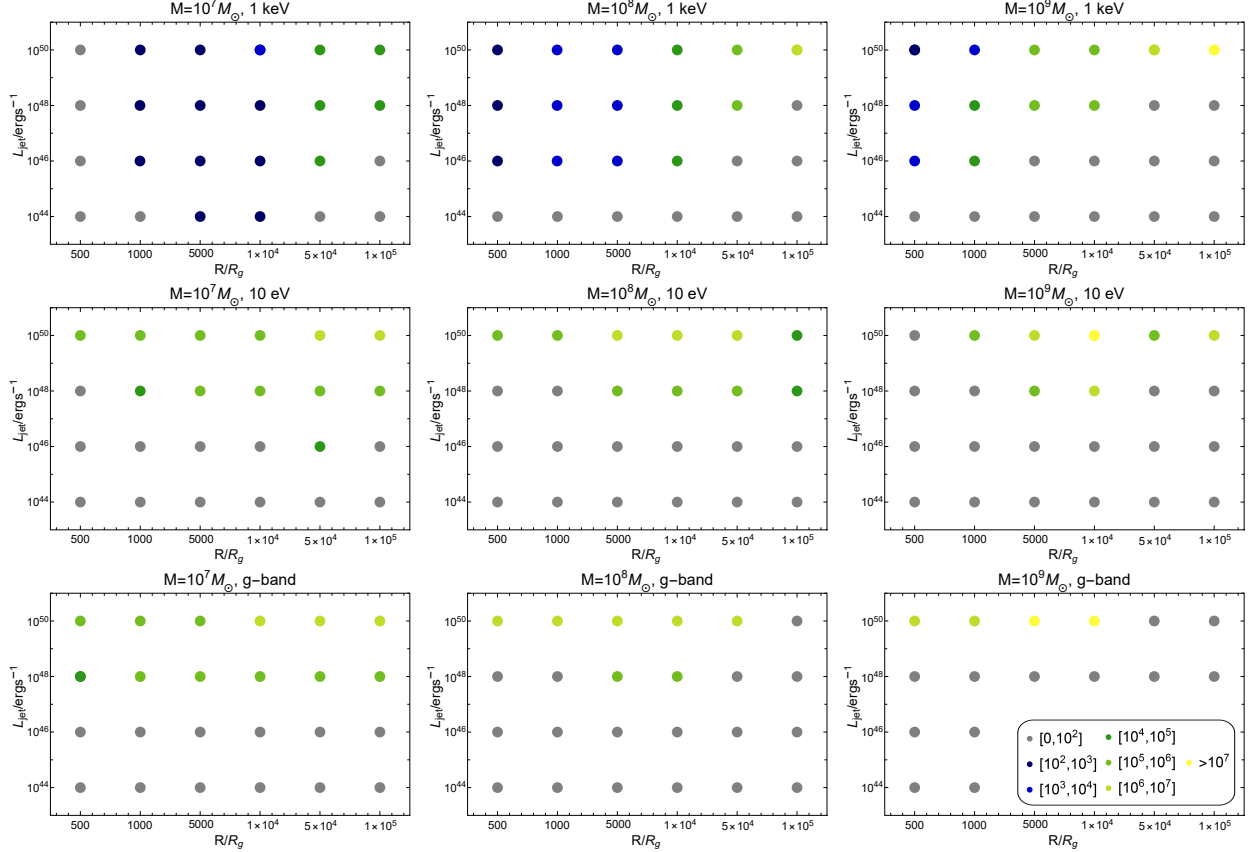


Figure 11. Duration of the observable flares in X-ray (first row), UV (second row), and optical (last row) bands produced by jets with varying powers embedded within different radius of AGN disks with central SMBH mass of $10^7 M_\odot$ (first column), $10^8 M_\odot$ (second column), and $10^9 M_\odot$ (last column). Dots in various colors represent the range of duration that the jet-cocoon system produced emission brighter than the AGN background radiation.

characteristics, with the first peak showing a sharper profile. Figure 11 depicts the duration of the observable soft X-ray flare across various parameter space regions. We find that the X-ray flares are generally observable, as their peak luminosities typically exceed the AGN background levels. However, their detectability additionally depends on both the luminosity distance of the source and telescope sensitivity. Exceptions occur when the jet power is substantially low, the SMBH mass is exceedingly high or the jet launching location is situated in the very inner region of the AGN disk. In most parameter spaces, the flare persists for $< O(10^5)$ s or a few days, signifying a short-lived event. Additionally, the flare duration increases with an increase in SMBH mass or AGN disk radius, attributable to the larger energy and volume of the jet-cocoon materials.

4.2.2. UV and Optical

The UV flares illustrated in the cases presented in Figure 9 are generally unobservable, as their peak luminosities are dimmer than the AGN background. The lack of detectability can be attributed to two main factors. First, the strong AGN radiation in the UV band masks weaker signals, making them difficult to distinguish. Second, when the observed temperature shifts into the UV band, both the disk-cocoon and the jet-cocoon, which responsible for the double-peak feature in cases 6 and 7, have undergone significant adiabatic expansion, leading to less energetic emissions, thereby reducing the detectability of the UV flares. Even so, an observable UV flare can be generated by the jet-cocoon system when the jet possesses sufficient power. For instance, as shown in Figure 9, a jet with a power of 10^{48} erg s $^{-1}$ in case 4 can produce a strong UV flare, which is primarily contributed by the disk-cocoon component. Owing to the high sensitivity of the advanced UV telescopes, even distant flares have the potential to be detected. The properties of the UV flare are systematically illustrated in Figure 11. Only jets with power $> 10^{46}$ erg s $^{-1}$ can produce observable UV flares, and the required power increases as the SMBH mass grows. An optimistic point is that the observable flare are

relatively long-lasting, with duration ranging from a few days to several tens of days. However, for jets with extremely high power, e.g., 10^{50} erg s $^{-1}$, their central engine must operate for at least $t_{j,\text{cri}}$ (see Figure 6) to support a successful jet breakout. It is quite challenging to satisfy this condition in astrophysical systems, and when $t_j < t_{j,\text{cri}}$, the choked jet-cocoon system would produce a dimmer flare (see below), potentially rendering it unobservable.

The properties of the optical flares resemble those of the UV flares. However, they exhibit weaker power and a more delayed peak time due to the lower corresponding emission temperature. As a result, optical flares are more difficult to observe, despite the observable flares lasting for a longer duration, as shown in Figure 11. Nonetheless, under favorable system parameter conditions, these flares can be captured by various telescopes, as demonstrated in Figure 9.

4.3. Choked jet emission

Table 2. Cases of choked jet in the AGN disk. The first five parameters have the same meaning as those in Table 1. t_j (in s) is the duration of the jet, where the first row is the continuous jet serving as a reference; t_{ch} (in s) is the jet choking time; t_{bre} (in s) is the breakout time of the successful jet or the jet-choked cocoon; z_{ch} (in H_d) is the height at which the jet becomes choked; $d_{\text{ch,bre}}$ (in H_d) and $\beta_{\text{ch,bre}}$ are the width and velocity of the cocoon breakout shell; $\theta_{\text{ch,bre}}$ is the opening angle of the jet-choked cocoon at its breakout; and β_{cut} is the maximum terminal velocity of the jet-choked jet-cocoon. The AGN disk adopts the [Sirko & Goodman \(2003\)](#) model, assuming a uniform vertical density profile.

case	M_{SMBH}	R_j	ρ_0	H_d	L_j	t_j	t_{ch}	t_{bre}	z_{ch}	$d_{\text{ch,bre}}$	$\beta_{\text{ch,bre}}$	$\theta_{\text{ch,bre}}$	β_{cut}
9	10^8	10^3	2.3×10^{-9}	3.5×10^{13}	10^{50}	–	–	1.3×10^3	–	4.6×10^{-5}	0.29	0.44	–
10	10^8	10^3	2.3×10^{-9}	3.5×10^{13}	10^{50}	1	95	5.0×10^4	0.08	1.7×10^{-3}	0.022	0.98	0.035
11	10^8	10^3	2.3×10^{-9}	3.5×10^{13}	10^{50}	10	307.9	1.3×10^4	0.25	5.3×10^{-4}	0.067	0.89	0.23
12	10^8	10^3	2.3×10^{-9}	3.5×10^{13}	10^{50}	100	1.0×10^3	1.7×10^3	0.80	1.1×10^{-4}	0.23	0.57	0.98

Table 2 presents four cases for investigating the jet choking of $t_{\text{ch}} < t_{\text{bre}}$, where case 9 represents a successful breakout jet and serves as a control example, while case 10 denotes a deeply choked jet, case 11 indicates a moderately choked jet, and case 12 corresponds to a barely choked jet. For jets with the same power, a shorter central engine active duration leads to a deeper choking, as the jet tail at engine shut-off would cover a shorter distance to catch up with its head. Both the velocity of the jet-choked cocoon at its breakout, $\beta_{\text{ch,bre}}$, and the cut-off terminal velocity of the jet-choked jet-cocoon, β_{cut} , decrease as z_{ch} decreases, indicating that the deeper choking leads to a less powerful cocoon, owing to an increased opening angle, a correspondingly larger cocoon volume and mass, and consequently a reduction in cocoon energy density.

The emission produced by the jet-choked cocoon system is weaker compared to that of a successful jet-cocoon system. As shown in Figure 12, the soft X-ray, UV, and optical flare emitted in case 9 are more luminous than the AGN background radiation. Therefore, this successful jet breakout event represents a multi-wavelength phenomenon. When the jet is barely choked in case 12, the overall properties of the cocoon have not changed significantly. A slightly longer breakout time and a modestly increased cocoon volume, together with a moderate decrease in cocoon velocity, result in a subtle deviation in the luminosity and temperature evolution of both cocoon components. Consequently, the flares are only slightly higher or lower than those associated with successful jets, rendering all flares in this case observable. However, the overall emission luminosity of the cocoon decreases substantially when the choking height is significantly deeper, as the cocoon becomes much weaker. As a result, in cases 10 and 11, the UV and optical flares produced are dimmer than those in cases 9 and 12, rendering them undetectable. Meanwhile, for a more deeply choked jet system, the jet-cocoon materials have been significantly weakened at the cocoon breakout. In case 11, the luminosity of the jet-cocoon emission decreases significantly, and since β_{cut} cannot result in the shock temperature reaching the X-ray band, no soft X-ray flare is generated. Moreover, in case 10, the choking is exceptionally deep, causing the freshly shocked disk materials to entirely drain the energy of the jet-cocoon, leading to its complete dissipation.

4.4. Specific astrophysical events

The potential existence of EM counterparts associated with GW events constitutes a distinctive property of binary black holes mergers occurring within the AGN disk. Indeed, several candidate optical flares have been reported to in association with LIGO GW events ([Graham et al. 2020, 2023](#)), where the host AGNs harbor massive SMBH with masses of $\sim 10^8 - 10^9 M_{\odot}$. If jets are the energy sources for radiation (e.g. [Tagawa et al. 2023b](#); [Rodríguez-Ramírez](#)

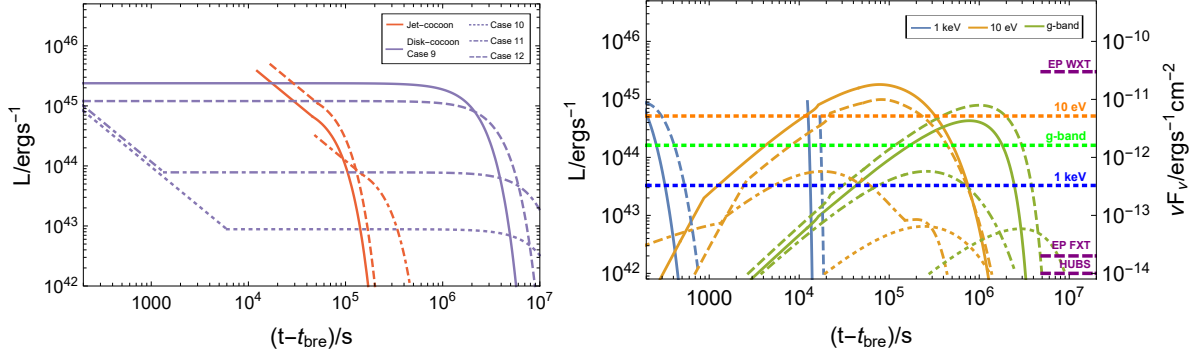


Figure 12. The evolution of bolometric luminosity for thermal emissions from the disk-cocoon and jet-cocoon components in cases 9, 10, 11, and 12, as well as the corresponding light curves in the X-ray, UV, and optical bands. The blue, orange, and green dotted lines illustrate the radiation of the background AGN. For a source luminosity distance of $d_L = 300$ Mpc, the dashed purple lines are identical to those in Figure 9.

et al. 2024; Chen & Dai 2024), and these flares are indeed the thermal emissions produced by the jet-cocoon system investigated in this work, then the jet powers are required to $\geq 10^{48}$ erg s $^{-1}$ (as shown in Figure 11), and the jets must persist for a sufficient duration $\gtrsim t_{j,\text{cri}}$ to ensure a successful breakout. These constraints on jet power and duration can facilitate the testing and investigation of the jet-launching mechanism of merger-remnant black holes. Meanwhile, the observation of optical flares is often accompanied by brighter soft X-rays and UV emissions. This suggests that merger-remnant black holes are multi-wavelength sources, and therefore multi-wavelength observation can serve as a crucial method to examine whether the candidate optical flares are the actual EM counterparts.

As a well-known EM counterpart for GW event, short GRBs arise from jets driven by the remnants of binary neutron star mergers or neutron star-black hole mergers. As short GRBs typically last less than a few seconds, the jets produced by these mergers within AGN disks are more likely to be choked unless the jets possess exceptional power and are launched at an extremely small inner disk radius, e.g., a location within a few hundred R_g around a less massive SMBH $\sim 10^7 M_\odot$, as illustrated in Figure 6. For short GRB jets that successfully break out of AGN disks, normal prompt emissions and afterglows can be produced (Perna et al. 2021a). Additionally, the cocoon material can contribute an extra early thermal emission component, which manifests as a UV flare and an optical flare lasting several days, while the X-ray flare is difficult to observe due to its short duration $\lesssim O(10^3)$ s. Conversely, when short GRB jets are choked in AGN harboring massive SMBH $\gtrsim 10^8 M_\odot$, no thermal flare are observable, let alone the absent normal prompt emission and afterglow. Only in cases where the jets are barely choked do thermal flares become observable, serving as the sole EM signals of the system when the subsequent non-thermal emission from the interaction between the cocoon material and the ambient gas beyond the AGN disk is weak.

The jet-driven long GRBs, which originate from the collapse of massive stars, constitute a class of strong transient sources. Stars can form in large numbers within the outer self-gravity unstable regions of AGN disks through fragmentation processes (Goodman 2003). However, whether these outer stars can migrate to the inner regions of AGN disks depends crucially on the still-debated efficiency of migration mechanisms (e.g. Bellovary et al. 2016; Grishin et al. 2024; Wu et al. 2024). Meanwhile, the dense inner regions of AGN disks are capable of capturing a substantial number of obliquely orbiting stars from the nuclear star cluster (Fabj et al. 2020). Moreover, the accretion processes of stars in the dense environments of these inner disk regions remain poorly understood by both theoretical models and numerical simulations (e.g. Chen et al. 2024b; Dittmann & Cantiello 2025; Fabj et al. 2025). To date, the comprehensive distribution and evolution of the embedded stellar population have not yet been thoroughly studied. Consequently, the specific statistical properties of AGN-disk-assisted long GRB jets remain inadequately constrained, particularly concerning their launch locations. Given that long GRBs feature more powerful and sustained jets, if they indeed occur within optically thick inner AGN disks, the generation of observable soft X-ray, UV, and optical thermal flares becomes more probable.

For any other astrophysical events embedded in AGN disks that launch jets, the properties of thermal emissions can be directly determined using the methods presented in this work, provided that the power and duration of the jets are specified by the central engine launching mechanism.

5. SUMMARY AND DISCUSSION

In this study, we have systematically investigated the dynamics and thermal emission properties of relativistic jets embedded in AGN disks. We calculated the evolution of the jet-cocoon system, by considering both successful breakout and choked jets, and analyzed the resulting thermal radiation from the jet-head shock breakout, disk-cocoon, and jet-cocoon components. Varying jet power, jet duration, and AGN disk parameters, we found that soft X-ray flares emerge as the most prominent observable signals, with duration ranging from $O(10^2)$ s to $O(10^5)$ s, frequently displaying double-peaked light curve morphology. UV flares produced in systems hosting ultra-powerful jets ($L_j \geq 10^{48}$ erg s $^{-1}$) that either successfully break out or are barely choked can be observed, possessing relatively longer duration ranging from several days to tens of days. Observable optical flares are the most challenging to produce; while they potentially distinguishable from AGN background, their luminosity remains lower than those of the other two types of flares, coupled with protracted emergence timescales and extended duration. Crucially, these multi-wavelength signatures establish a diagnostic paradigm for identifying whether the observed optical flares are genuine EM counterparts to binary black hole merger GW events within AGN disks, particularly through their characteristic temporal sequencing where optical flares consistently follow precursor UV and soft X-ray emissions. Moreover, these thermal flares represent an essential component of the early observable signatures for the breaking-out embedded GRB jets, and may even constitute the sole detectable signature when the jet is choked within the AGN disk.

Our study primarily examines the thermal emissions produced by the initially opaque jet-cocoon system during the early stage following the breakout of the jet and cocoon. Upon emergence from the AGN disk, the relativistic jet (if it persists) and accompanying cocoon materials interact with the ambient gas above the AGN disk photosphere, such as in the broad-line region, through collisionless shocks that generate non-thermal radiation. By contrast, jets launched from the outer regions of the AGN disk exhibit a distinct behavior. In these optically-thin environments where the disk total optical depth satisfies $\tau_d(z=0) < 1$, the shocked jet-head undergoes collisionless processes that directly produce non-thermal radiation, bypassing the formation of a cocoon structure. The detailed analysis of the system evolution and the resulting non-thermal emissions, while beyond the current scope, will be studied elsewhere.

Additionally, it should be noted that we have assumed that the jets originate from the mid-plane of an undistributed AGN disk and propagate perpendicular to the disk plane. Despite being reasonable and representative, the assumptions are somewhat oversimplified. Below, we briefly discuss the implications of relaxing these idealized conditions. First, prior to or during jet launching, persistent accretion of disk materials by the central engine potentially alter the gas distribution along the jet propagation path. For instance, if accretion leads to significant large-scale gas accumulation around the central engine, the enhanced ambient density would exert stronger deceleration on the jet. Conversely, if accretion-driven outflow feedback dominates, a low-density cavity could form along the jet trajectory (e.g. Wang et al. 2021a; Chen et al. 2023; Tagawa et al. 2024), significantly reducing environmental resistance and enabling the jet to propagate more freely. Second, vertical displacement of the launching site from the disk midplane introduces asymmetric propagation distances: compared to the mid-plane case, the jet facing the nearer disk surface encounters a reduced amount of AGN disk material, while the opposing jet must traverse a greater disk thickness. For a successful breakout jet, a larger propagation distance implies more energy being deposited into the cocoon, thereby enhancing the brightness of the cocoon-produced emission. Conversely, midplane-choked jets might achieve breakout if launched closer to the disk surface. Finally, jet inclination adds additional complexity: oblique trajectories require longer breakout paths through the disk medium. Consequently, successful inclined jets would transfer more energy to cocoon, potentially generating brighter thermal flares, while jets originally choked at the disk mid-plane would experience deeper choking.

6. ACKNOWLEDGMENTS

This work was supported by the National Natural Science Foundation of China (grant No. 12393812), the National SKA Program of China (grant No. 2020SKA0120302), and the Strategic Priority Research Program of the Chinese Academy of Sciences (grant NO. XDB0550300).

APPENDIX

A. ADIABATIC EVOLUTION OF RELATIVISTIC BREAKOUT SHELL

The acceleration of a relativistic optically thick shell during the planar phase following its breakout can be described by (Pan & Sari 2006; Nakar & Sari 2012)

$$\gamma = \gamma_h \left(\frac{t}{t_0} \right)^{\frac{\sqrt{3}-1}{2}}, \quad (\text{A1})$$

where $t_0 \sim 1/\kappa\rho c$. When the entire internal energy is adiabatically converted into kinetic energy, the shell reaches its final Lorentz factor (Johnson & McKee 1971; Pan & Sari 2006)

$$\gamma_f = \gamma_h^{\sqrt{3}+1}, \quad (\text{A2})$$

and the acceleration ends at

$$t_f = t_0 \gamma_h^{3+\sqrt{3}}. \quad (\text{A3})$$

The transition from planar to spherical evolution occurs when the shell's width matches its initial radius at the shell's radius doubling, which is around

$$t_{h,s} \simeq \frac{(\Sigma_h/\pi)^{\frac{1}{2}}}{c}. \quad (\text{A4})$$

A critical Lorentz factor $\gamma_{h,s}$ is determined by the condition $t_f = t_{h,s}$:

$$\gamma_{h,s} = \left[\frac{(\Sigma_h/\pi)^{\frac{1}{2}}}{t_0 c} \right]^{\frac{1}{3+\sqrt{3}}}, \quad (\text{A5})$$

which can divide the shell evolution into two distinct modes. For $\gamma_h \leq \gamma_{h,s}$, acceleration terminates during the planar phase and the corresponding shell final Lorentz factor is γ_f . Otherwise, acceleration ends in the spherical phase.

The sustainability of adiabatic evolution significantly depends on the optical depth of the shell. Initially, Numerous shock-generated electron-positron pairs prevent photons from escaping and regulate the rest-frame downstream temperature to $T'_h = 200$ keV. During the adiabatic expansion, the shell undergoes continuous cooling with its temperature following $T' \propto V'^{-\frac{1}{3}}$, where V' represents its volume. As the pair density drops sharply when the temperature decreases below 100 keV (e.g. Svensson 1984), the optical depth of the breakout shell keeps decreasing until the pair density becomes negligible at approximate $T'_{th} = 50$ keV. At this point, photons can diffuse out of the breakout shell, as its original $\tau_d \lesssim 1$.

For $\gamma_h < \gamma_{h,s}$, the shell volume increases as $V' \propto t/\gamma$ and $V' \propto t$ during and after its acceleration. During the spherical phase, $V' \propto t^3$. Therefore, when the shell becomes transparent in these three phases, the corresponding timescales are

$$t_{h,th} = \begin{cases} t_0 \left(\frac{T'_h}{T'_{th}} \right)^{3+\sqrt{3}}, & t_{h,th} \leq t_f \\ t_0 \left(\frac{T'_h}{T'_{th}} \right)^3 \gamma_h^{\sqrt{3}}, & t_f < t_{h,th} \leq t_{h,s} \\ t_0 \left(\frac{T'_h}{T'_{th}} \right) \gamma_h^{\frac{\sqrt{3}}{3}} \left(\frac{t_0}{t_{h,s}} \right)^{\frac{1}{3}}, & t_{h,th} > t_{h,s} \end{cases} \quad (\text{A6})$$

and the corresponding Lorentz factors of the shell are

$$\gamma_{h,th} = \begin{cases} \gamma_h \left(\frac{T'_h}{T'_{th}} \right)^{\sqrt{3}}, & \frac{T'_h}{T'_{th}} < \gamma_h \\ \gamma_f, & \gamma_h \leq \frac{T'_h}{T'_{th}}, \left(\frac{t_0 T'_h{}^3}{t_{h,s} T'_{th}{}^3} \right)^{-\frac{\sqrt{3}}{3}} \\ \gamma_f, & \left(\frac{t_0 T'_h{}^3}{t_{h,s} T'_{th}{}^3} \right)^{-\frac{\sqrt{3}}{3}} < \gamma_h \leq \frac{T'_h}{T'_{th}} \end{cases} \quad (\text{A7})$$

For $\gamma_h > \gamma_{h,s}$, the acceleration persists throughout the entire planar phase and ends in the spherical phase. In such case, Equation (A1) is no longer applicable. However, given the rapid expansion of volume, we simplistically assume

that the breakout shell becomes transparent around the beginning of spherical phase. Therefore, the transparency timescale and the Lorentz factor of the breakout shell are

$$\begin{cases} t_{\text{h,th}} = t_0 \left(\frac{T_{\text{h}}'}{T_{\text{th}}'} \right)^{3+\sqrt{3}}, & \gamma_{\text{h,th}} = \gamma_{\text{h}} \left(\frac{T_{\text{h}}'}{T_{\text{th}}'} \right)^{\sqrt{3}}, & t_{\text{h,th}} \leq t_{\text{h,s}} \\ t_{\text{h,th}} \simeq t_{\text{h,s}}, & \gamma_{\text{h,th}} \simeq \gamma_{\text{h}} \left(\frac{t_0}{t_{\text{h,s}}} \right)^{\frac{1-\sqrt{3}}{2}}. & t_{\text{h,th}} \gtrsim t_{\text{h,s}} \end{cases} \quad (\text{A8})$$

B. EMISSION PROPERTIES OF DISK-COCOON IN STRATIFIED AGN DISK

When the disk-cocoon vertically expands within a disk characterized by a decreasing density profile of the form $\rho(z) \propto (z_{\text{c,bre}} - z)^n$, where $z_{\text{c,bre}}$ is the shock breakout height of the disk cocoon, the velocity of its forefront shock accelerates as $\beta_{\text{c,h}} \propto \rho^{-\mu}$, where $\mu \approx 0.19$ (Sakurai 1960). Although neither the isothermal nor the polytropic disk strictly adheres to a power-law decay density profile, the disk density profile can be locally approximated as a power-law one by matching the reduction rate at a specific height, thereby assigning an effective power-law index n_{eff} for different $z_{\text{c,bre}}$ (Grishin et al. 2021). Setting H_{d} as the lower limit height of the effective power-law density profile, the density profile can be expressed as $\rho_{\text{eff}}(z) = \rho(H_{\text{d}})[(z_{\text{c,bre}} - z)/(z_{\text{c,bre}} - H_{\text{d}})]^{n_{\text{eff}}}$, and n_{eff} can be determined by $d\rho_{\text{eff}}(z)/dz = d\rho(z)/dz$. Therefore, for isothermal disk,

$$n_{\text{eff,iso}} = \frac{z_{\text{c,bre}} - H_{\text{d}}}{H_{\text{d}}}, \quad (\text{B1})$$

and for polytropic disk,

$$n_{\text{eff,poly}} = \frac{6}{5} \frac{z_{\text{c,bre}} - H_{\text{d}}}{H_{\text{d}}}. \quad (\text{B2})$$

The acceleration occurs at approximately $z_{\text{acc,iso}} \sim (3/2\mu)^{1/2} H_{\text{d}} = 2.8H_{\text{d}}$ for isothermal disk and $z_{\text{acc,poly}} \sim (1/6 + 2\mu/3)^{-\frac{1}{2}} H_{\text{d}} = 1.8H_{\text{d}}$ for polytropic disk (Grishin et al. 2021). When $z_{\text{c,bre}} < z_{\text{acc}}$, we disregard shock acceleration and model the luminosity and temperature of the disk-cocoon emission in the same manner as the uniform disk case, i.e., Equation (29), (30), and (31). Conversely, we follow Nakar & Sari (2010) to investigate the emission evolution.

By estimating the typical velocity of the shocked disk-cocoon shell at z_{acc} as $\beta_{\text{c,d}} \simeq (E_{\text{c}}/M_{\text{c}}c^2)^{\frac{1}{2}}$, for the breakout shell, its velocity is accelerated to $\beta_{\text{c,bre}} \simeq \beta_{\text{c,d}}[\rho(z_{\text{c,bre}})/\rho(z_{\text{acc}})]^{-\mu}$, and thereby the breakout height can be determined using $\tau_{\text{d}}(z_{\text{c,bre}}) = 1/\beta_{\text{c,bre}}$. The luminosity evolution can be described by (Nakar & Sari 2010; Piro et al. 2021)

$$L_{\text{c}}(t) = \begin{cases} L_{\text{c,bre}} \exp \left[1 - \frac{t_{\text{c,bre}}}{t} \right], & t \leq t_{\text{c,bre}} \\ L_{\text{c,bre}} \left(\frac{t}{t_{\text{c,bre}}} \right)^{-\frac{4}{3}}, & t_{\text{c,bre}} < t \leq t_{\text{c,pla}} \\ L_{\text{c,bre}} \left(\frac{t_{\text{c,pla}}}{t_{\text{c,bre}}} \right)^{-\frac{4}{3}} \left(\frac{t}{t_{\text{c,pla}}} \right)^{-\frac{2.28n-2}{3(1.19n+1)}}, & t_{\text{c,pla}} < t \leq t_{\text{c,d}} \\ L_{\text{c,d}} \exp \left[-\frac{1}{2} \left(\frac{t^2}{t_{\text{c,d}}^2} - 1 \right) \right], & t > t_{\text{c,d}} \end{cases} \quad (\text{B3})$$

where $n = n_{\text{eff,iso}}$ or $n_{\text{eff,poly}}$ for specific disk vertical density profile; $L_{\text{c,bre}}$ and $t_{\text{c,bre}}$ are calculated by substituting $\beta_{\text{c,bre}}$ into Equation (24) and (25); $t_{\text{c,d}}$ represents the time when photons initially coupled with the accelerated shells have sufficiently diffused out, leading to subsequent emission originating from the unaccelerated material, which can be calculated by replacing H_{d} with z_{acc} in Equation (26); the corresponding emission luminosity is determined using Equation (27). Still, for simplicity, we directly connect the planar phase with $t < t_{\text{c,pla}}$ and the disk-cocoon cooling phase with $t > t_{\text{c,d}}$.

For $\beta_{\text{c,bre}} < 0.03$, the observed temperature evolves as

$$T_{\text{BB,c}}(t) \propto \begin{cases} \exp \left[1 - \frac{t_{\text{c,bre}}}{t} \right]^{\frac{1}{4}}, & t \leq t_{\text{c,bre}} \\ \left(\frac{t}{t_{\text{c,bre}}} \right)^{-\frac{2(9n+5)}{3(17n+9)}}, & t_{\text{c,bre}} < t \leq t_{\text{c,pla}} \\ \left(\frac{t}{t_{\text{c,pla}}} \right)^{-\frac{18.48n^2+20.69n+6}{(1.19n+1)(22.32n+17)}}, & t_{\text{c,pla}} < t \leq t_{\text{c,d}} \\ \exp \left[-\frac{1}{2} \left(\frac{t^2}{t_{\text{c,d}}^2} - 1 \right) \right]^{\frac{4.33n+3}{4(2.79n+2.13)}} \left(\frac{t}{t_{\text{c,d}}} \right)^{-\frac{1.3(n+1)}{2.79n+2.13}}, & t > t_{\text{c,d}} \end{cases} \quad (\text{B4})$$

where $T_c(t_{c,\text{bre}}) = T_{\text{BB},\text{cbre}} = (18\rho\beta_{c,\text{bre}}^2 c^2/7a)^{\frac{1}{4}}$, and the evolution during $t \leq t_{c,d}$ refers to Nakar & Sari (2010). For photons diffusing out of a series of shells with different mass, velocity, and optical depth, the observed temperature is determined at the so called color radius, where $\eta = 1$ (Nakar & Sari 2010). Within this color radius framework, we investigate the temperature evolution during $t > t_{c,d}$. For a spherically expanding shell, its thermal coupling coefficient $\eta \propto T_{\text{BB},\text{sh}}^{\frac{7}{2}} \rho_{\text{sh}}^{-2} t_{\text{diff,sh}}^{-1} \propto L_c^{\frac{7}{8}} m_{\text{sh}}^{-\frac{17}{8} - \frac{1.33n}{2(n+1)}} t^{\frac{7}{2}}$, where the parameters follow that the thermal equilibrium temperature $T_{\text{BB},\text{sh}} \propto L_c^{\frac{1}{4}} m_{\text{sh}}^{\frac{1}{4}} r_{\text{sh}}^{-1}$, the shell density $\rho_{\text{sh}} \propto m_{\text{sh}} r_{\text{sh}}^{-3}$, the diffusion of shell $t_{\text{diff,sh}} \propto m_{\text{sh}} r_{\text{sh}}^{-1}$, the shell radius $r_{\text{sh}} \propto \beta_{\text{sh}} t$, and the shell velocity $\beta_{\text{sh}} \propto m^{-\frac{0.19n}{n+1}}$. Therefore, the properties of the color shell evolve following $m_{\text{cl}} \propto (L_c^{\frac{7}{8}} t^{\frac{7}{2}})^{\frac{n+1}{2.79n+2.13}}$, $\beta_{\text{cl}} \propto (L_c^{\frac{7}{8}} t^{\frac{7}{2}})^{-\frac{0.19n}{2.79n+2.13}}$, and $r_{\text{cl}} \propto (L_c^{\frac{7}{8}} t^{\frac{7}{2}})^{-\frac{0.19n}{2.79n+2.13}} t$. The resulting observed temperature is $T_{\text{BB,c}} \propto L_c^{\frac{1}{4}} m_{\text{cl}}^{\frac{1}{4}} r_{\text{cl}}^{-1}$, i.e., the last row of Equation (B4).

For $\beta_{c,\text{bre}} > 0.03$, the observed temperature evolves as

$$T_{\text{Com,c}}(t) \propto \begin{cases} \exp\left[1 - \frac{t_{c,\text{bre}}}{t}\right]^2 \left(\frac{t}{t_{c,\text{bre}}}\right)^{-2}, & t \leq t_{c,\text{bre}} \\ \left(\frac{t}{t_{c,\text{bre}}}\right)^{-\frac{2}{3}}, & t_{c,\text{bre}} < t \leq t_{c,\text{pla}} \\ \left(\frac{t}{t_{c,\text{pla}}}\right)^{-\frac{21.26n+1}{3(1.19n+1)}}, & t_{c,\text{pla}} < t \leq t_{c,\text{th1}} \\ \left(\frac{t}{t_{c,\text{th1}}}\right)^{-\frac{3n+2}{6(1.19n+1)}}, & t_{c,\text{th1}} < t \leq t_{c,\text{th2}} \\ \left(\frac{t}{t_{c,\text{th2}}}\right)^{-\frac{18.48n^2+20.69n+6}{(1.19n+1)(22.32n+17)}}, & t_{c,\text{th2}} < t \leq t_{c,d} \\ \exp\left[-\frac{1}{2}\left(\frac{t^2}{t_{c,d}^2} - 1\right)\right]^{\frac{4.33n+3}{4(2.79n+2.13)}} \left(\frac{t}{t_{c,d}}\right)^{-\frac{1.3(n+1)}{2.79n+2.13}}, & t > t_{c,d} \end{cases}, \quad (\text{B5})$$

where $T_{\text{Com,c}}(t_{c,\text{bre}}) = T_{\text{Com,cbre}}$, which is calculated via substituting $\beta_{c,\text{bre}}$ in Equation (18) to replace β_{h} , and the evolution during $t \leq t_{c,d}$ refers to Nakar & Sari (2010). $t_{c,\text{th1}}$ and $t_{c,\text{th2}}$ represent two critical time, where

$$t_{c,\text{th1}} = t_{c,\text{pla}} \left[\eta_{c,\text{bre}} \left(\frac{t_{c,\text{bre}}}{t_{c,\text{pla}}}\right)^{\frac{1}{6}} \right]^{\frac{3(1.19n+1)}{9.88n+5}}, \quad (\text{B6})$$

$$t_{c,\text{th2}} = t_{c,\text{pla}} \left[\eta_{c,\text{bre}} \left(\frac{t_{c,\text{bre}}}{t_{c,\text{pla}}}\right)^{\frac{1}{6}} \right]^{\frac{6(1.19n+1)}{12.48n+1}}. \quad (\text{B7})$$

When $t < t_{c,\text{th1}}$, the observed emission temperature is out of thermal equilibrium and exhibits Comptonization; when $t_{c,\text{th1}} < t < t_{c,\text{th2}}$, emission reaches thermal equilibrium, and the observed temperature is determined by the shell from which photons escape; when $t > t_{c,\text{th2}}$, photons interact with outer shells during diffusion, modifying their properties, and the observed temperature is determined by the outermost shell that is in thermal equilibrium, the evolution reverts to Equation (B4). Taking Equation (B5) as the benchmark, the relative magnitudes among different timescales alter the specific temperature evolution. For $t_{c,\text{th1}} < t_{c,d} \leq t_{c,\text{th2}}$, since the outer shells do not affect the emission, the temperature evolution after $t_{c,d}$ follows that of an isolated shell, where $T \propto L_c^{\frac{1}{4}} t^{-\frac{1}{2}}$. When $t_{c,d} < t_{c,\text{th1}}$, similarly, after $t_{c,d}$, we consider the cooling of an isolated shell. Given that the temperature is initially out of thermal equilibrium, it evolves as $T \propto t^{-1}$ until thermal equilibrium is reached, after which $T \propto L_c^{\frac{1}{4}} t^{-\frac{1}{2}}$. Furthermore, if the emission approaches thermal equilibrium during the planar phase, its temperature will evolve in accordance with Equation (32).

C. TEMPERATURE EVOLUTION OF NEWTONIAN JET-COCOON

To ascertain whether the jet-cocoon emission is in thermal equilibrium, we calculate the thermal coupling coefficient of the Newtonian jet-cocoon shells. Before undergoing spherical expansion, materials need first escape from the initial jet-cocoon cylinder. Assuming a shell is located at a distance $d_{\text{cj}} = f_d z_{\text{bre}}$ from the breakout height, the escaping time

can be estimated as $t_{\text{esc}} = d_{\text{cj}}/\beta_{\text{cj}}c$. Thus, for the shell with $\beta_{\text{cj},s}$, its initial thermal coupling coefficient is

$$\eta_{\text{esc},s} = \frac{aT_{\text{BB},\text{cj}0}^{\frac{7}{2}}}{1.05 \times 10^{37} k \rho_{\text{cj},s}^2 t_{\text{esc}}} = \frac{E_{\text{cj}}^{\frac{7}{8}} V_{\text{cj}}^{\frac{9}{8}} \beta_{\text{cj},s} c}{A m_{\text{cj},s}^2 f_{\text{d}} z_{\text{bre}}}, \quad (\text{C1})$$

where $A = 1.05 \times 10^{37} k/a^{\frac{1}{8}}$, $\rho_{\text{cj},s} = m_{\text{cj},s}/V_{\text{cj},s}$. For heavier jet-cocoon material with $\beta_{\text{cj},i} < \beta_{\text{cj},s}$, $T_{\text{BB},\text{cj}}$ is nearly constant due to energy density equalization in jet-cocoon, its density is estimated as $\rho_{\text{cj},i}/\rho_{\text{cj},s} = m_{\text{cj},i}d_{\text{cj},s}/m_{\text{cj},s}d_{\text{cj},i}$, and its escaping time is approximately $t_{\text{esc},i}/t_{\text{esc},s} = d_{\text{cj},s}\beta_{\text{cj},i}/d_{\text{cj},i}\beta_{\text{cj},s}$. As $E \propto V_{\text{cj},\beta}$, the spatial distribution of the jet-cocoon material follows $dE/d\log\beta_{\text{cj}} \propto dd(>v)/d\log\beta_{\text{cj}}$, leading to depth evolves as $d_{\text{cj},i}/d_{\text{cj},s} = (f_{\Gamma\beta} z_{\text{bre}}/d_{\text{cj},s})\log[\beta_{\text{cj},s}/\beta_{\text{cj},i}] + 1$. Consequently, the thermal coupling coefficient for heavier shell is given by

$$\eta_{\text{esc},i} = \eta_{\text{esc},s} \left(\frac{m_{\text{cj},i}}{m_{\text{cj},s}} \right)^{-\frac{2s+3}{s+1}} \left(\frac{f_{\Gamma\beta} z_{\text{bre}}}{d_{\text{cj},s}} \log \left[\frac{\beta_{\text{cj},s}}{\beta_{\text{cj},i}} \right] + 1 \right). \quad (\text{C2})$$

During the spherical expansion phase, the shell radius increases as $r_{\text{cj}} = \beta_{\text{cj}}t$. Consequently, the properties of materials outside the luminosity shell evolve according to $T_{\text{BB},\text{cj}} \propto L_{\text{cj}}^{\frac{1}{4}} m_{\text{cj}}^{\frac{1}{4}} r_{\text{cj}}^{-1}$, $\rho_{\text{cj}} \propto m_{\text{cj}} r_{\text{cj}}^{-3}$, and $t_{\text{cj}} \propto m_{\text{cj}} r_{\text{cj}}^{-1}$, which results in the thermal coupling coefficient evolving as

$$\eta_{\text{cj}}(m_{\text{cj}} > m_{\text{cj},s}) = \eta_{\text{cj},s} \left(\frac{m_{\text{cj}}}{m_{\text{cj},s}} \right)^{-\frac{17s+45}{8(s+1)}} \left(\frac{t}{t_{\text{cj},s}} \right)^{\frac{7(s+1)}{2(s+2)}}, \quad (\text{C3})$$

where

$$\eta_{\text{cj},s} = \eta_{\text{esc},s} \left(\frac{t_{\text{cj},s}}{t_{\text{esc},s}} \right)^{\frac{3}{2}}, \quad (\text{C4})$$

is the thermal coupling coefficient of the shell with $\beta_{\text{cj},s}$ at $t_{\text{cj},s}$, derived from the adiabatic expansion of the shell from $t_{\text{esc},s}$ to $t_{\text{cj},s}$. Since the thermal coupling becomes weaker during the spherical phase, $\eta_{\text{esc},s}$ governs the temperature properties of the jet-cocoon emission.

When $\eta_{\text{esc},s} \leq 1$, the emission is in thermal equilibrium, and its temperature evolves as

$$T_{\text{BB},\text{cj}}(t) \propto \begin{cases} \left(\frac{t}{t_{\text{cj},s}} \right)^{-\frac{2(5s^2+27s+50)}{(s+2)(17s+45)}}, & t_{\text{cj},s} < t \leq t_{\text{th,ph}} \\ \left(\frac{t}{t_{\text{th,ph}}} \right)^{-\frac{s^2+5s+8}{2(s+2)(s+3)}}, & t_{\text{th,ph}} < t \leq t_{\text{sph,end}} \\ \exp \left[-\frac{1}{2} \left(\frac{t^2}{t_{\text{sph,end}}^2} - 1 \right) \right]^{\frac{1}{4}} \left(\frac{t}{t_{\text{sph,end}}} \right)^{-\frac{s+1}{2(s+3)}}, & t > t_{\text{sph,end}} \end{cases}, \quad (\text{C5})$$

where $T_{\text{BB},\text{cj}}(t_{\text{cj},s}) = T_{\text{BB},\text{cjs}}$, and $T_{\text{BB},\text{cjs}}$ is the thermal equilibrium temperature at $t_{\text{cj},s}$, which is given by

$$T_{\text{BB},\text{cjs}} = \left(\frac{L_{\text{cj},s}}{ac\beta_{\text{cj},s} r_{\text{cj},s}^2} \right)^{\frac{1}{4}}. \quad (\text{C6})$$

By setting $\eta_{\text{cj}} = 1$ in Equation (C3), the properties of the color shell, which determines the observed temperature (Nakar & Sari 2010), can be achieved. The mass outside this shell is

$$m_{\text{cj},\text{cl}} = m_{\text{cj},s} \eta_{\text{cj},s}^{\frac{8(s+1)}{17s+45}} \left(\frac{t}{t_{\text{cj},s}} \right)^{\frac{28(s+1)^2}{(s+2)(17s+45)}}, \quad (\text{C7})$$

and as $m(>v) \propto v^{-(s+1)}$, the color radius is given by

$$r_{\text{cj},\text{cl}} = r_{\text{cj},s} \eta_{\text{cj},s}^{-\frac{8}{17s+45}} \left(\frac{t}{t_{\text{cj},s}} \right)^{\frac{17s^2+51s+62}{(s+2)(17s+45)}}. \quad (\text{C8})$$

Nevertheless, when photons diffuse out of the jet-cocoon photosphere, material's influence on the emission becomes negligible, leading to the failure of the color shell, and we assume that the observed temperature is determined by the photosphere radius, which is at $\kappa m/4\pi r_{\text{cj,ph}}^2 = 1$, i.e.,

$$r_{\text{cj,ph}} = r_{\text{cj,s}} \beta_{\text{cj,s}}^{-\frac{1}{s+3}} \left(\frac{t}{t_{\text{cj,s}}} \right)^{\frac{s+1}{s+3}}. \quad (\text{C9})$$

The transition occurs at $r_{\text{cj,cl}} = r_{\text{cj,ph}}$, where the corresponding time is

$$t_{\text{th,ph}} = t_{\text{s,cj}} \beta_{\text{cj,s}}^{-\frac{(s+2)(17s+45)}{6s^2+46s+96}} \eta_{\text{cj,s}}^{\frac{4(s+2)(s+3)}{3s^2+23s+48}}. \quad (\text{C10})$$

When $t < t_{\text{th,ph}}$, the observed temperature evolves following $T_{\text{BB,cj}} \propto L_{\text{cj}}^{\frac{1}{4}} m_{\text{cj,cl}}^{\frac{1}{4}} r_{\text{cj,cl}}^{-1}$, thereby yielding the first row of Equation (C5). Similarly, when $t > t_{\text{th,ph}}$, the observed temperature follows $T_{\text{BB,cj}} \propto L_{\text{cj}}^{\frac{1}{4}} r_{\text{cj,ph}}^{-1}$, leading to the last two rows of Equation (C5).

For the jet-cocoon with $\eta_{\text{esc,s}} > 1$, its temperature is initially out of thermal equilibrium. The Compton modified temperature can be calculated using $T_{\text{esc}} \xi(T_{\text{esc}})^2 = T_{\text{BB,cj0}} \eta_{\text{esc}} (T_{\text{BB,cj0}})^2$ (Nakar & Sari 2010), where the Comptonization correction factor is

$$\xi(T) \approx \max \left\{ 1, \frac{1}{2} \ln(y_{\text{max}}) [1.6 + \ln(y_{\text{max}})] \right\}, \quad (\text{C11})$$

with $y_{\text{max}} = 3 (\rho/10^{-9} \text{ g cm}^{-3})^{-\frac{1}{2}} (T/100 \text{ eV})^{\frac{9}{4}}$. After adiabatic cooling, the observed temperature at $t_{\text{cj,s}}$ is

$$T_{\text{Com,cjs}} \simeq T_{\text{esc,s}} \frac{V_{\text{cj,s}}^{\frac{1}{3}}}{r_{\text{cj,s}}}. \quad (\text{C12})$$

The temperature evolution is given by

$$T_{\text{Com,cj}}(t) \propto \begin{cases} \left(\frac{t}{t_{\text{cj,s}}} \right)^{-\frac{9s+12}{s+2}}, & t_{\text{cj,s}} < t \leq t_{\text{cj,th1}} \\ \left(\frac{t}{t_{\text{cj,th1}}} \right)^{-\frac{s+1}{2(s+2)}}, & t_{\text{cj,th1}} < t \leq t_{\text{cj,th2}} \\ \left(\frac{t}{t_{\text{cj,th2}}} \right)^{-\frac{2(5s^2+27s+50)}{(s+2)(17s+45)}}, & t_{\text{cj,th2}} < t \leq t_{\text{th,ph}} \\ \left(\frac{t}{t_{\text{th,ph}}} \right)^{-\frac{s^2+5s+8}{2(s+2)(s+3)}}, & t_{\text{th,ph}} < t \leq t_{\text{sph,end}} \\ \exp \left[-\frac{1}{2} \left(\frac{t^2}{t_{\text{sph,end}}^2} - 1 \right) \right]^{0.25} \left(\frac{t}{t_{\text{sph,end}}} \right)^{-\frac{s+1}{2(s+3)}}, & t > t_{\text{sph,end}} \end{cases}, \quad (\text{C13})$$

where $T_{\text{cj}}(t_{\text{cj,s}}) = T_{\text{Com,cjs}}$. Similar to the disk-cocoon case, two critical times $t_{\text{cj,th1}} \equiv t(\eta_{\text{esc}} = 1)$ and $t_{\text{cj,th2}} \equiv t(\eta_{\text{cj}} = 1)$ calculating at the luminosity shell are

$$t_{\text{cj,th1}} \simeq t_{\text{cj,s}} \eta_{\text{esc,s}}^{\frac{s+2}{2(2s+3)}}, \quad (\text{C14})$$

$$t_{\text{cj,th2}} = t_{\text{cj,s}} \eta_{\text{cj,s}}^{\frac{4(s+2)}{3s+31}}. \quad (\text{C15})$$

During $t_{\text{cj,s}} < t \leq t_{\text{cj,th1}}$, the observed temperature is determined by the luminosity shell, given by $T_{\text{Com,cj}} \simeq \eta_{\text{esc}}^2 T_{\text{BB,0}} (V_{\text{cj},\beta}^{\frac{1}{3}}/r_{\text{cj}}) \propto t^{-\frac{9s+12}{s+2}}$. The adiabatic cooling of the luminosity shell governs the temperature evolution when $t_{\text{cj,th1}} < t \leq t_{\text{cj,th2}}$, resulting in $T_{\text{Com,cj}} \propto L_{\text{cj}}^{\frac{1}{4}} m_{\text{cj}}^{\frac{1}{4}} r_{\text{cj}}^{-1} \propto t^{-\frac{s+1}{2(s+2)}}$. After $t > t_{\text{cj,th2}}$, the temperature evolution follows Equation (C5).

Furthermore, if the Compton modified temperature is exceedingly high, the newly generated pairs would suppress the temperature to approximately 200 keV when materials leave the jet-cocoon cylinder. During the adiabatic spherical expansion, the pair effect becomes negligible in trapping photons when the temperature decreases to ~ 50 keV (Nakar & Sari 2012), at a time given by

$$t_{\text{cj,np}}(\beta_{\text{cj}}) \simeq \frac{V_{\text{cj},\beta}^{\frac{1}{3}}}{\beta_{\text{cj}} c} \frac{200 \text{ keV}}{50 \text{ keV}} = \frac{4V_{\text{cj},\beta}^{\frac{1}{3}}}{\beta_{\text{cj},c}}. \quad (\text{C16})$$

For $t_{\text{cj,np}}(\beta_{\text{cj,s}}) < t_{\text{cj,s}}$, photons escape and produce emission at diffusion radius $r_{\text{cj,s}}$ with the observed temperature given by

$$T_{\text{pair,cjs}} = 200 \text{ keV} \frac{V_{\text{cj,s}}^{\frac{1}{3}}}{r_{\text{cj,s}}}. \quad (\text{C17})$$

As the initial temperatures of the luminosity shells remain nearly constant due to the regulation of pairs, the observed temperature evolves following $T_{\text{pair,cj}} \propto r_{\text{cj}}^{-1}$ of the luminosity shell, i.e.,

$$T_{\text{pair,cj}}(t) = T_{\text{pair,cjs}} \left(\frac{t}{t_{\text{cj,s}}} \right)^{-\frac{s}{s+2}}, \quad t_{\text{cj,s}} < t \leq t_{\text{esp,np}} \quad (\text{C18})$$

where $t_{\text{esp,np}}$ is the time when the initial Comptonized temperature T_{esc} decreases to 50 keV with few pair production. By neglecting the evolution of ξ , $T_{\text{esc}} \simeq T_{\text{esc,s}}(\eta_{\text{esc}}/\eta_{\text{esc,s}})^2$, and thereby

$$t_{\text{esp,np}} \simeq t_{\text{cj,s}} \left(\frac{T_{\text{esc,s}}}{50 \text{ keV}} \right)^{\frac{s+2}{4(2s+3)}}. \quad (\text{C19})$$

When $t > t_{\text{esp,np}}$, the observed temperature follows Equation (C13) by substituting $t_{\text{esp,np}}$ for $t_{\text{cj,s}}$. However, for $t_{\text{cj,np}}(\beta_{\text{cj,s}}) > t_{\text{cj,s}}$, the luminosity shell must propagate to a radius larger than $r_{\text{cj,s}}$ to produce emission with a temperature of 50 keV. The condition continues until the velocity of the luminosity shell satisfies $t_{\text{cj,np}} = t_{\text{cj}}$, which is given by

$$\beta_{\text{cj,50keV}} = \frac{\kappa f_{\Gamma\beta} E_{\text{cj}}}{32\pi c^2 V_{\text{cj,\beta}}^{\frac{2}{3}}}, \quad (\text{C20})$$

and the corresponding time is

$$t_{\text{cj,50keV}} = \frac{128\pi c V_{\text{cj,\beta}}}{\kappa f_{\Gamma\beta} E_{\text{cj}}}. \quad (\text{C21})$$

Thus, the observed temperature evolves as

$$T_{\text{pair,cj}}(t) = \begin{cases} 50 \text{ keV}, & t_{\text{cj,np}}(\beta_{\text{cj,s}}) < t \leq t_{\text{cj,50keV}} \\ 50 \text{ keV} \left(\frac{t}{t_{\text{cj,50keV}}} \right)^{-\frac{s}{s+2}}, & t_{\text{cj,50keV}} < t \leq t_{\text{esp,np}} \end{cases} \quad (\text{C22})$$

Still, when $t > t_{\text{esp,np}}$, the observed temperature follows Equation (C13) by substituting $t_{\text{esp,np}}$ for $t_{\text{cj,s}}$.

REFERENCES

- Abbott, B. P., Abbott, R., Abbott, T. D., et al. 2017, *PhRvL*, 119, 161101. doi:10.1103/PhysRevLett.119.161101
- Abbott, B. P., Abbott, R., Abbott, T. D., et al. 2017, *ApJL*, 848, L12. doi:10.3847/2041-8213/aa91c9
- Abbott, R., Abbott, T. D., Abraham, S., et al. 2020, *PhRvL*, 125, 101102. doi:10.1103/PhysRevLett.125.101102
- Arnett, W. D. 1982, *ApJ*, 253, 785. doi:10.1086/159681
- Begelman, M. C. & Cioffi, D. F. 1989, *ApJL*, 345, L21. doi:10.1086/185542
- Bellm, E. 2014, *The Third Hot-wiring the Transient Universe Workshop*, 27. doi:10.48550/arXiv.1410.8185
- Bellovary, J. M., Mac Low, M.-M., McKernan, B., et al. 2016, *ApJL*, 819, 2, L17. doi:10.3847/2041-8205/819/2/L17
- Bromberg, O. & Tchekhovskoy, A. 2016, *MNRAS*, 456, 1739. doi:10.1093/mnras/stv2591
- Bromberg, O., Nakar, E., Piran, T., et al. 2011, *ApJ*, 740, 100. doi:10.1088/0004-637X/740/2/100
- Budnik, R., Katz, B., Sagiv, A., et al. 2010, *ApJ*, 725, 63. doi:10.1088/0004-637X/725/1/63
- Burrows, D. N., Hill, J. E., Nousek, J. A., et al. 2005, *SSRv*, 120, 165. doi:10.1007/s11214-005-5097-2
- Cenko, S. B., Frail, D. A., Harrison, F. A., et al. 2010, *ApJ*, 711, 641. doi:10.1088/0004-637X/711/2/641
- Chatzopoulos, E., Wheeler, J. C., & Vinko, J. 2012, *ApJ*, 746, 121. doi:10.1088/0004-637X/746/2/121

- Chen, K., Ren, J., & Dai, Z.-G. 2023, *ApJ*, 948, 136.
doi:10.3847/1538-4357/acc45f
- Chen, K. & Dai, Z.-G. 2024, *ApJ*, 961, 206.
doi:10.3847/1538-4357/ad0dfd
- Chen, Y.-X. & Lin, D. N. C. 2024, *ApJ*, 967, 88.
doi:10.3847/1538-4357/ad3c3a
- Chen, Y.-X., Jiang, Y.-F., Goodman, J., et al. 2024, *ApJ*, 974, 1, 106. doi:10.3847/1538-4357/ad6dd4
- Dai, L., McKinney, J. C., Roth, N., et al. 2018, *ApJL*, 859, L20. doi:10.3847/2041-8213/aab429
- Delfavero, V., Ford, K. E. S., McKernan, B., et al. 2024, arXiv:2410.18815. doi:10.48550/arXiv.2410.18815
- Dittmann, A. J. & Cantiello, M. 2025, *ApJ*, 979, 2, 245. doi:10.3847/1538-4357/ad9e92
- Eisenberg, M., Gottlieb, O., & Nakar, E. 2022, *MNRAS*, 517, 582. doi:10.1093/mnras/stac2184
- Epstein-Martin, M., Tagawa, H., Haiman, Z., et al. 2025, *MNRAS*, 537, 3396. doi:10.1093/mnras/staf237
- Fabj, G., Nasim, S. S., Caban, F., et al. 2020, *MNRAS*, 499, 2608. doi:10.1093/mnras/staa3004
- Fabj, G., Dittmann, A. J., Cantiello, M., et al. 2025, *ApJ*, 981, 16. doi:10.3847/1538-4357/ada896
- Frank, J., King, A., & Raine, D. J. 2002, *Accretion Power in Astrophysics*, by Juhan Frank and Andrew King and Derek Raine, pp. 398. ISBN 0521620538. Cambridge, UK: Cambridge University Press, February 2002., 398
- Gangardt, D., Trani, A. A., Bonnerot, C., et al. 2024, *MNRAS*, 530, 3689. doi:10.1093/mnras/stae1117
- Gilbaum, S. & Stone, N. C. 2022, *ApJ*, 928, 191. doi:10.3847/1538-4357/ac4ded
- Goodman, J. 2003, *MNRAS*, 339, 937. doi:10.1046/j.1365-8711.2003.06241.x
- Gottlieb, O., Bromberg, O., Singh, C. B., et al. 2020, *MNRAS*, 498, 3320. doi:10.1093/mnras/staa2567
- Gottlieb, O., Nakar, E., & Bromberg, O. 2021, *MNRAS*, 500, 3511. doi:10.1093/mnras/staa3501
- Graham, M. J., Ford, K. E. S., McKernan, B., et al. 2020, *PhRvL*, 124, 251102. doi:10.1103/PhysRevLett.124.251102
- Graham, M. J., McKernan, B., Ford, K. E. S., et al. 2023, *ApJ*, 942, 99. doi:10.3847/1538-4357/aca480
- Grishin, E., Bobrick, A., Hirai, R., et al. 2021, *MNRAS*, 507, 156. doi:10.1093/mnras/stab1957
- Grishin, E., Gilbaum, S., & Stone, N. C. 2024, *MNRAS*, 530, 2, 2114. doi:10.1093/mnras/stae828
- Hamidani, H. & Ioka, K. 2021, *MNRAS*, 500, 627. doi:10.1093/mnras/staa3276
- Harrison, R., Gottlieb, O., & Nakar, E. 2018, *MNRAS*, 477, 2128. doi:10.1093/mnras/sty760
- Huang, B.-Q., Liu, T., Li, X.-Y., et al. 2024, *ApJ*, 967, 67. doi:10.3847/1538-4357/ad3d54
- Irwin, C. M., Nakar, E., & Piran, T. 2019, *MNRAS*, 489, 2844. doi:10.1093/mnras/stz2268
- Ishibashi, W. & Gröbner, M. 2024, *MNRAS*, 529, 883. doi:10.1093/mnras/stae569
- Jansen, F., Lumb, D., Altieri, B., et al. 2001, *A&A*, 365, L1. doi:10.1051/0004-6361:20000036
- Jermyn, A. S., Dittmann, A. J., Cantiello, M., et al. 2021, *ApJ*, 914, 105. doi:10.3847/1538-4357/abfb67
- Johnson, M. H. & McKee, C. F. 1971, *PhRvD*, 3, 858. doi:10.1103/PhysRevD.3.858
- Kang, H. D., Perna, R., Lazzati, D., et al. 2025, *The Open Journal of Astrophysics*, 8, 23. doi:10.33232/001c.131902
- Kathirgamaraju, A., Li, H., Ryan, B. R., et al. 2024, *ApJ*, 972, 101. doi:10.3847/1538-4357/ad63a3
- Kato, S., Fukue, J., & Mineshige, S. 2008, *Black-Hole Accretion Disks — Towards a New Paradigm —*, 549 pages, including 12 Chapters, 9 Appendices, ISBN 978-4-87698-740-5, Kyoto University Press (Kyoto, Japan), 2008.
- Katz, B., Budnik, R., & Waxman, E. 2010, *ApJ*, 716, 781. doi:10.1088/0004-637X/716/1/781
- Kim, Y. & Most, E. R. 2024, arXiv:2409.12359. doi:10.48550/arXiv.2409.12359
- Kulkarni, S. R., Harrison, F. A., Grefenstette, B. W., et al. 2021, arXiv:2111.15608.
- Lazzati, D., Soares, G., & Perna, R. 2022, *ApJL*, 938, L18. doi:10.3847/2041-8213/ac98ad
- Lei, L., Zhu, Q.-F., Kong, X., et al. 2023, *Research in Astronomy and Astrophysics*, 23, 035013. doi:10.1088/1674-4527/acb877
- Levinson, A. & Nakar, E. 2020, *PhR*, 866, 1. doi:10.1016/j.physrep.2020.04.003
- Liang, E.-W., Racusin, J. L., Zhang, B., et al. 2008, *ApJ*, 675, 528. doi:10.1086/524701
- LSST Science Collaboration, Abell, P. A., Allison, J., et al. 2009, arXiv:0912.0201. doi:10.48550/arXiv.0912.0201 doi:10.48550/arXiv.2111.15608
- Matzner, C. D. 2003, *MNRAS*, 345, 575. doi:10.1046/j.1365-8711.2003.06969.x
- McKernan, B., Ford, K. E. S., Lyra, W., et al. 2012, *MNRAS*, 425, 460. doi:10.1111/j.1365-2966.2012.21486.x
- McKernan, B., Ford, K. E. S., O’Shaughnessy, R., et al. 2020, *MNRAS*, 494, 1203. doi:10.1093/mnras/staa740
- McKernan, B., Ford, K. E. S., & O’Shaughnessy, R. 2020, *MNRAS*, 498, 4088. doi:10.1093/mnras/staa2681
- Morsony, B. J., Lazzati, D., & Begelman, M. C. 2007, *ApJ*, 665, 569. doi:10.1086/519483

- Nakar, E., Piran, T., & Sari, R. 2005, *ApJ*, 635, 516.
doi:10.1086/497296
- Nakar, E. & Sari, R. 2010, *ApJ*, 725, 904.
doi:10.1088/0004-637X/725/1/904
- Nakar, E. & Sari, R. 2012, *ApJ*, 747, 88.
doi:10.1088/0004-637X/747/2/88
- Nakar, E. & Piro, A. L. 2014, *ApJ*, 788, 193.
doi:10.1088/0004-637X/788/2/193
- Nakar, E. & Piran, T. 2017, *ApJ*, 834, 28.
doi:10.3847/1538-4357/834/1/28
- Pais, M., Piran, T., & Nakar, E. 2023, *MNRAS*, 519, 1941.
doi:10.1093/mnras/stac3640
- Pan, M. & Sari, R. 2006, *ApJ*, 643, 416. doi:10.1086/502958
- Perna, R., Lazzati, D., & Cantiello, M. 2021, *ApJL*, 906, L7. doi:10.3847/2041-8213/abd319
- Perna, R., Tagawa, H., Haiman, Z., et al. 2021, *ApJ*, 915, 10. doi:10.3847/1538-4357/abfdb4
- Piro, A. L., Haynie, A., & Yao, Y. 2021, *ApJ*, 909, 209.
doi:10.3847/1538-4357/abe2b1
- Qin, Y., Liang, E.-W., Liang, Y.-F., et al. 2013, *ApJ*, 763, 15. doi:10.1088/0004-637X/763/1/15
- Ray, M., Lazzati, D., & Perna, R. 2023, *MNRAS*, 521, 4233. doi:10.1093/mnras/stad816
- Rodríguez-Ramírez, J. C., Bom, C. R., Fraga, B., et al. 2024, *MNRAS*, 527, 6076. doi:10.1093/mnras/stad3575
- Rowan, C., Whitehead, H., & Kocsis, B. 2024, arXiv:2412.12086. doi:10.48550/arXiv.2412.12086
- Sagiv, I., Gal-Yam, A., Ofek, E. O., et al. 2014, *AJ*, 147, 79. doi:10.1088/0004-6256/147/4/79
- Sakurai, A. 1960, *Commun. Pure Appl. Math.*, 13, 353. doi:10.1088/0004-637X/774/1/79
- Sapir, N., Katz, B., & Waxman, E. 2013, *ApJ*, 774, 79. doi:10.1088/0004-637X/774/1/79
- Shakura, N. I. & Sunyaev, R. A. 1973, *A&A*, 24, 337
- Shang, Z., Brotherton, M. S., Wills, B. J., et al. 2011, *ApJS*, 196, 2. doi:10.1088/0067-0049/196/1/2
- Sirko, E. & Goodman, J. 2003, *MNRAS*, 341, 501. doi:10.1046/j.1365-8711.2003.06431.x
- Suzuki, A., Irwin, C. M., & Maeda, K. 2024, *PASJ*, 76, 863. doi:10.1093/pasj/psae055
- Svensson, R. 1982, *ApJ*, 258, 335. doi:10.1086/160082
- Svensson, R. 1984, *MNRAS*, 209, 175. doi:10.1093/mnras/209.2.175
- Syer, D., Clarke, C. J., & Rees, M. J. 1991, *MNRAS*, 250, 505. doi:10.1093/mnras/250.3.505
- Tagawa, H., Haiman, Z., & Kocsis, B. 2020, *ApJ*, 898, 25. doi:10.3847/1538-4357/ab9b8c
- Tagawa, H., Kimura, S. S., Haiman, Z., et al. 2022, *ApJ*, 927, 41. doi:10.3847/1538-4357/ac45f8
- Tagawa, H., Kimura, S. S., Haiman, Z., et al. 2023, *ApJL*, 946, L3. doi:10.3847/2041-8213/acc103
- Tagawa, H., Kimura, S. S., Haiman, Z., et al. 2023, *ApJ*, 950, 13. doi:10.3847/1538-4357/acc4bb
- Tagawa, H., Kimura, S. S., Haiman, Z., et al. 2024, *ApJ*, 966, 21. doi:10.3847/1538-4357/ad2e0b
- Tan, J. C., Matzner, C. D., & McKee, C. F. 2001, *ApJ*, 551, 946. doi:10.1086/320245
- Thompson, T. A., Quataert, E., & Murray, N. 2005, *ApJ*, 630, 167. doi:10.1086/431923
- Urrutia, G., De Colle, F., & López-Cámara, D. 2023, *MNRAS*, 518, 5145. doi:10.1093/mnras/stac3401
- Wang, J.-M., Liu, J.-R., Ho, L. C., et al. 2021, *ApJL*, 911, L14. doi:10.3847/2041-8213/abee81
- Wang, J.-M., Liu, J.-R., Ho, L. C., et al. 2021, *ApJL*, 916, L17. doi:10.3847/2041-8213/ac0b46
- Wang, Y.-H., Lazzati, D., & Perna, R. 2022, *MNRAS*, 516, 5935. doi:10.1093/mnras/stac1968
- Weaver, T. A. 1976, *ApJS*, 32, 233. doi:10.1086/190398
- Weisskopf, M. C., Tananbaum, H. D., Van Speybroeck, L. P., et al. 2000, *Proc. SPIE*, 4012, 2. doi:10.1117/12.391545
- Woosley, S. E. 1993, *ApJ*, 405, 273. doi:10.1086/172359
- Woosley, S. E. & Bloom, J. S. 2006, *ARA&A*, 44, 507. doi:10.1146/annurev.astro.43.072103.150558
- Wu, Y., Chen, Y.-X., & Lin, D. N. C. 2024, *MNRAS*, 528, 1, L127. doi:10.1093/mnras/sl4d183
- Xue, L., Tagawa, H., Haiman, Z., et al. 2025, arXiv:2504.19570. doi:10.48550/arXiv.2504.19570
- Yang, Y., Bartos, I., Gayathri, V., et al. 2019, *PhRvL*, 123, 181101. doi:10.1103/PhysRevLett.123.181101
- Yang, Y., Bartos, I., Haiman, Z., et al. 2019, *ApJ*, 876, 122. doi:10.3847/1538-4357/ab16e3
- Yang, Y., Bartos, I., Fragione, G., et al. 2022, *ApJL*, 933, L28. doi:10.3847/2041-8213/ac7c0b
- Yuan, W., Zhang, C., Chen, Y., et al. 2022, *Handbook of X-ray and Gamma-ray Astrophysics*, 86. doi:10.1007/978-981-16-4544-0_151-1
- Zhang, B. 2018, *The Physics of Gamma-Ray Bursts by Bing Zhang*. ISBN: 978-1-139-22653-0. Cambridge University Press, 2018. doi:10.1017/9781139226530
- Zhang, H.-H., Zhu, J.-P., & Yu, Y.-W. 2024, *ApJ*, 976, 63. doi:10.3847/1538-4357/ad8139
- Zhang, Y.-N., Li, C., Xu, D., et al. 2022, *Experimental Astronomy*, 53, 3, 1053. doi:10.1007/s10686-022-09856-7